Geochemistry, Geophysics, Geosystems

RESEARCH ARTICLE
10.1029/2020GC009488

# Magmatic Processes in the East African Rift System: Insights From a 2015–2020 Sentinel-1 InSAR Survey

F. Albino[1] and J. Biggs[1]

[1]COMET, School of Earth Sciences, University of Bristol, Bristol, UK

**Key Points:**

- InSAR survey (2015–2020) detects deformation at 14 Holocene volcanoes in the East African Rift System
- Episodes of uplift are detected on several centers with no historical eruptions (Corbetti, Suswa)
- New subsidence signals are caused by lava compaction at Kone and geothermal activity at Olkaria

**Supporting Information:**

- Supporting Information S1

**Correspondence to:**
F. Albino,
fa17101@bristol.ac.uk

**Citation:**
Albino, F., & Biggs, J. (2021). Magmatic processes in the East African Rift System: Insights from a 2015–2020 Sentinel-1 InSAR survey. *Geochemistry, Geophysics, Geosystems*, *22*, e2020GC009488. https://doi.org/10.1029/2020GC009488

Received 19 OCT 2020
Accepted 13 DEC 2020



**Abstract** The East African Rift System (EARS) is composed of around 78 Holocene volcanoes, but relatively little is known about their past and present activity. This lack of information makes it difficult to understand their eruptive cycles, their roles in continental rifting and the threat they pose to the population. Although previous InSAR surveys (1990–2010) showed sign of unrest, the information about the dynamics of the magmatic systems remained limited by low temporal resolution and gaps in the data set. The Sentinel-1 SAR mission provides open-access acquisitions every 12 days in Africa and has the potential to produce long-duration time series for studying volcanic ground deformation at regional scale. Here, we use Sentinel-1 data to provide InSAR time series along the EARS for the period 2015–2020. We detect 18 ground deformation signals on 14 volcanoes, of which six are located in Afar, six in the Main Ethiopian Rift, and two in the Kenya-Tanzanian Rift. We detected new episodes of uplift at Tullu Moje (2016) and Suswa (mid-2018), and enigmatic long-lived subsidence signals at Gada Ale and Kone. Subsidence signals are related to a variety of mechanisms including the posteruptive evolution of magma reservoirs (e.g., Alu-Dallafila), the compaction of lava flows (e.g., Nabro), and pore-pressure changes related to geothermal or hydrothermal activity (e.g., Olkaria). Our results show that ~20% of the Holocene volcanoes in the EARS deformed during this 5-years snapshot and demonstrate the diversity of processes occurring.

## 1. Introduction

The East African Rift System (EARS) contains 78 volcanoes with records of Holocene activity (Global Volcanism Program, 2013) (Figure 1), but little is known about their past or present behavior. This lack of information makes it difficult to understand their eruptive cycles, their role in continental rifting or assess the threat they pose to the rapidly growing population. To fill this gap, it is necessary to collect information about past eruptions and to characterize present activity. On one hand, field studies can provide constraints on eruptive history, using tephrostratigraphy to estimate the age and magnitude of Quaternary eruptions (see Fontijn et al. (2018) for a review). On the other hand, geophysical ground-based observations help constrain the distribution of magmatic and/or hydrothermal fluids along the rift (Gottsmann et al., 2020; Kendall et al., 2005; Samrock et al., 2018; Wilks et al., 2017). Satellite observations, and especially radar interferometry (InSAR), can routinely produce ground displacements maps over large areas and therefore are well-suited for carrying out surveys of magmatic systems on the scale of entire plate boundaries. Such surveys provide a snapshot of the dynamics of magmatic systems and their eruptive cycles (Delgado et al., 2016; Lu & Dzurisin, 2014; Pyle et al., 2013; Reath et al., 2020).

The ERS (1997–2000) and Envisat satellites (2003–2010) were instrumental in characterizing a series of dike intrusions in the EARS (Table 1), carrying out regional-scale InSAR surveys in the Main Ethiopian Rift (MER) and Kenyan Rift (Biggs et al., 2009a, 2011) and producing a three-dimensional velocity field of the Afar region (Pagli et al., 2014). These systematic studies were the first to identify unrest at several caldera systems, and have motivated subsequent ground-based studies (e.g., Gottsmann et al., 2020; Wilks et al., 2017). However, these early InSAR studies were limited by low temporal resolution (3–4 images per year for Envisat and only a few images for ERS and JERS) and the lack of continuity between missions which resulted in gaps of several months in the time series.

The launch of the European Union radar constellation Sentinel-1 in 2014 represents the first opportunity to produce high resolution, long-duration time series of volcano deformation. Systematic acquisitions are

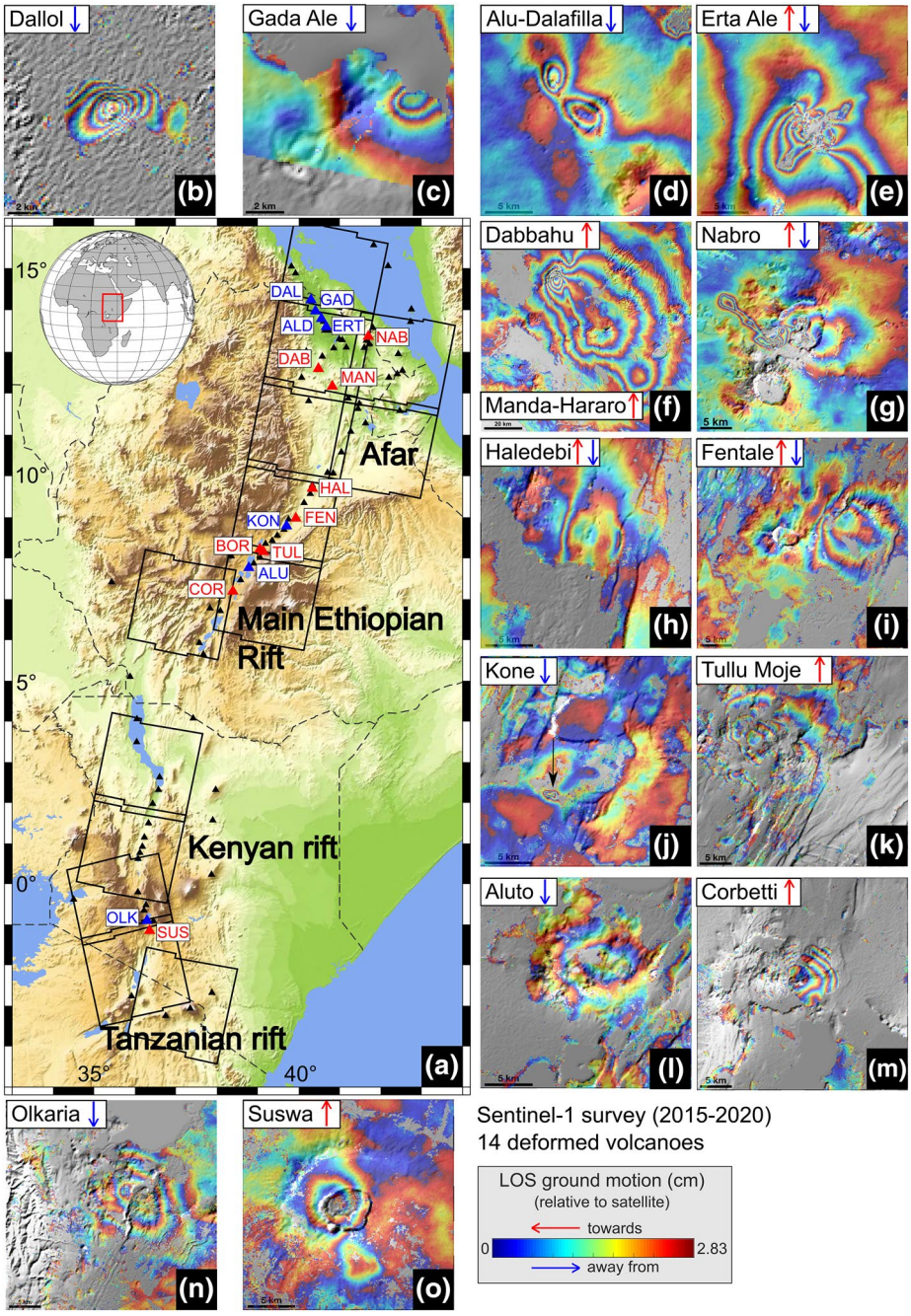


**Figure 1.** (a) Topographic map showing the Holocene active volcanoes (Global Volcanism Program, 2013) located along the East African Rift System from Eritrea to Tanzania. Colored triangles indicate the volcanoes with deformation recorded during our 2015–2020 Sentinel-1 survey (red = motion toward satellite; blue = motion away from satellite): DAL = Dallol, GAD = Gada Ale, ALD = Alu-Dalafilla, ERT = Erta Ale, NAB = Nabro, DAB = Dabbahu, MAN = Manda-Hararo, HAL = Haludebi, FEN = Fentale, KON = Kone, BOR = BORA, TUL = Tullu Moje, ALU = Aluto, COR = Corbetti, OLK = Olkaria, SUS = Suswa. (b–o) Small insets showing the cumulative wrapped interferograms for the deformed volcanoes, with the arrows indicating the sign of motion.

**Table 1**
*Ground Deformation Signals Detected by Previous InSAR Surveys in the Afar Depression, the Main Ethiopian Rift (MER), and the Kenyan-Tanzanian Rift*

| Volcano | Last eruption | Satellite | Period of unrest | Amplitude (cm) | Source | Reference |
|---|---|---|---|---|---|---|
| Alu-Dalafilla | 2008 | Envisat | 2008 | +9 | Sill | Pagli et al. (2012) |
| | | ALOS | 2008 | −100 − 190 | Reservoir | Pagli et al. (2012) |
| Ayelu | 1928 | ERS-1 | 2000 | +5 | Dike | Keir et al. (2011) |
| Dabbahu | 2005 | Envisat | 2005 | +150 − 200 | Dike/reservoir | Wright et al. (2006) |
| | | Envisat | 2005–2009 | | dike | Grandin et al. (2010a) |
| | | Envisat | 2006–2009 | +35 + 80 | dike/viscous | Hamling et al. (2014) |
| Dallol | 2011 | Envisat | 2004 | −30 + 17 | Dike/fault/reservoir | Nobile et al. (2012) |
| Erta Ale | 2017 | Envisat | 2005–2010 | −20 + 30 | Dike | Barnie et al. (2016a) |
| | | S1 | 2014–2019 | | Dike/reservoir | Moore et al. (2019) and Xu et al. (2017) |
| | | ALOS2 CSK S1 | 2017–2019 | −9 | Reservoir | Xu et al. (2020) |
| Gade Ale | None | ERS-1 | 1993–1996 | −11 | Sill/fault | Amelung et al. (2000) |
| Nabro | 2011 | TSX CSK | 2011 | −40 | Dike/fault | Goitom et al. (2015) |
| | | TSX | 2011–2012 | −20 | Reservoir | Hamlyn et al. (2014) |
| Tendaho | | Envisat | 2008–2010 | −10 | Geothermal | Temtime et al. (2018) |
| Aluto | None | ERS Envisat | 2004 | +15 | Reservoir | Biggs et al. (2011) |
| | | ERS Envisat | 2008 | +10 | Reservoir | Biggs et al. (2011) |
| Corbetti | None | ERS Envisat | 2008–2009 | +4 | Reservoir | Biggs et al. (2011) |
| | | ALOS CSK S1 | 2009–2017 | +50 | Reservoir | Lloyd et al. (2018b) |
| Fentale | 1810 | CSK S1 | 2015 | +7 | Dike | Temtime et al. (2020) |
| Haledebi | None | ERS Envisat | 2008–2010 | +4 − 5 | Reservoir/fault | Biggs et al. (2011) |
| Tullu Moje | 1900 | ERS Envisat | 2008–2010 | +5 | Reservoir | Biggs et al. (2011) |
| Gelai | None | Envisat ALOS | 2007 | +42 | Dike | Baer et al. (2008) |
| | | Envisat | 2007–2008 | −6 | Dike cooling | Biggs et al. (2013) |
| Lengai | Continuing | Envisat | 2007 | | Dike | Biggs et al. (2013) |
| | | | 2008 | −7 | Reservoir | Biggs et al. (2013) |
| Longonot | None | ERS Envisat | 2004–2006 | +9 | Reservoir | Biggs et al. (2009a) |
| Menengai | None | ERS Envisat | 1997–2000 | −3 | Reservoir | Biggs et al. (2009a) |
| Paka | None | ERS Envisat | 2006–2007 | +21 | Reservoir | Biggs et al. (2009a) |
| Suswa | None | ERS Envisat | 1997–2000 | −5 | Reservoir | Biggs et al. (2009a) |

planned for the next 20 years with a repeat interval of 12–24 days in Africa, with data released in near real-time. Some recent InSAR studies have already taken advantage of the Sentinel-1 data set to investigate diking events in the EARS, including the 2015 Fentale intrusion (Temtime et al., 2020) and the 2017 Erta Ale intrusion (Moore et al., 2019; Xu et al., 2017, 2020), and to analyze long-lived unrest at silicic centers such as Corbetti caldera (Lloyd et al., 2018b).

Here, we systematically report results from the first 5 years of Sentinel-1 data along the East African Rift System. Using the LiCSAR automated system (Lazecký et al., 2020), we process about 4,000 interferograms along the EARS with a large majority (~85%) generated from descending tracks (Supplementary Material Table S1). In total, we produce Sentinel-1 InSAR time series over 64 Holocene active volcanoes between October 2014 and January 2020 (Albino & Biggs, 2021) (Supplementary Material Tables S2–S4). We identify ground deformation at 14 volcanoes and describe the spatial and temporal characteristics of each signal.

## 2. Data Set and Methods

Radar interferometry (InSAR) maps ground displacements using the phase delays between two radar images of the same geographical area. Sentinel-1 operated by the European Space Agency (ESA) delivers free radar images under the EU Copernicus programme. At the time of the writing, the mission consists of two satellites: Sentinel-1A (launched in 2014) and Sentinel-1B (launched in 2016). Both satellites carry C-band antennas (wavelength = 5.6 cm) operating in TOPS mode (Terrain Observation by Progressive Scans) (Yagüe-Martínez et al., 2016) and together they provided a minimum revisit time over Africa of 24 days from January 2015 to January 2017 and 12 days from January 2017 to December 2019.

We process Sentinel-1 SAR data from 13 frames covering the EARS (Supplementary Material Table S1) for a 5-year period between October 2014 and December 2019, using the LiCSAR processing system (Lazecký et al., 2020). LiCSAR is built on the GAMMA software package (Werner et al., 2000) and automatically generates the three shortest temporal baseline interferograms for each acquisition at a spatial resolution of 0.001° × 0.001° (~111 m at the equator). More than 4,000 interferograms were processed covering 64 Holocene active volcanoes (Supplementary Material Tables S2–S4). All the processed data (coherence and interferograms) are freely available at https://comet.nerc.ac.uk/comet-lics-portal/. To reduce the computing time, we crop the LiCSAR coherence maps and unwrapped interferograms to a geographical region 0.5° × 0.5° centered on the location of each volcano (Global Volcanism Program, 2013). We use the method of Yip et al. (2019) to select a representative reference pixel. As for all automatically generated data sets, the LiCSAR data set contains some poor-quality data that originated from processing issues (e.g., missing bursts, misregistration) or limitations of the InSAR method (e.g., temporal decorrelation) and these products are removed prior to the analysis.

Atmospheric signals are a major challenge when using InSAR for volcano monitoring as they can mask deformation, or even lead to misinterpretation at high-relief edifices (Beauducel et al., 2000; Yip et al., 2019). Such signals are caused by variability in atmospheric conditions (e.g., pressure, temperature, water vapor) and are typically considered to be composed of a stratified component that correlates with topography and a turbulent component that is spatially correlated over wavelengths of ~10 km (Lohman & Simons, 2005) and is randomly distributed in time. Therefore, the impact of atmospheric noise is expected to be important for stratovolcanoes located in humid, tropical climates such as Central America and South East Asia (Albino et al., 2020; Ebmeier et al., 2013). Tropospheric signals can be mitigated using (i) empirical methods based on the correlation between phase and elevation (Beauducel et al., 2000; Delacourt et al., 1998; Remy et al., 2003), (ii) weather-based models (Bekaert et al., 2015; Parker et al., 2015; Pinel et al., 2011; Stephens et al., 2020), or (iii) both (Albino et al., 2020). Because most of the EARS lies in desert and semiarid climates and the volcanoes are generally low relief, the Sentinel-1 interferograms contain low levels of atmospheric noise. We apply atmospheric corrections using the empirical method only for volcanoes showing strong correlations between phase and elevation. In total, this is 15 of the 64 volcanoes processed: seven volcanoes in Afar (Alid, Ma-Alalta, Dabbayra, Manda-Gargori, Asavyo, Nabro, and Dubbi), three in the Main Ethiopian Rift (Bishoftu, Butajiri Silti field, and Tullu Moje) and five in the Kenyan-Tanzania Rift (Emuruangogolak, Silali, Paka, Korosi, and Ol Doinyo Lengai). In addition, we remove a plane from the uncorrected interferograms to account for any long-wavelength atmospheric or orbital errors.

We use a least-squares approach to retrieve displacement maps at each date of acquisition (Schmidt & Bürgmann, 2003; Usai, 2003) and use a linear approximation to derive the velocity. No smoothing or filtering is applied during the inversion process. We automatically plot the time series of displacements at three specific locations: (A) a nondeforming point located outside the ground deformation signal, (B) the volcano center, defined by the Smithsonian Global Volcanism Program (Global Volcanism Program, 2013), and (C) the point of maximum magnitude displacements (negative or positive depending of the sign of unrest). For the time series, the value plotted and the corresponding uncertainties are derived from the average and the standard deviation calculated on a 5 × 5 window (e.g., area of ~0.25 $km^2$) centered on each location. We chose to show the time series at the location (C), because the choice of volcano center (B) may be arbitrary, especially for large calderas, fissures swarms, and complex volcanic systems and deformation signals are often offset from the volcanic edifice (Ebmeier et al., 2018).

## 3. Results

Our 2015–2020 Sentinel-1 InSAR survey of the East African Rift System (EARS) detected 18 deformation signals at 14 volcanic centers (Figure 1) of which only three (Erta Ale, Corbetti, Fentale) had previously been reported (Lloyd et al., 2018b; Moore et al., 2019; Temtime et al., 2020; Xu et al., 2017, 2020). We group the deformation signals into five classes: (1) restless calderas, (2) dike intrusions, (3) deformation following eruption or intrusion, (4) subsidence and seasonal signals associated with pore-pressure changes, and (5) lava flow subsidence. In this section, we detail the characteristics (e.g., amplitude, rate, duration) of each deformation signal. We briefly discuss the possible causative mechanisms, but detailed modeling is beyond the scope of this study.

### 3.1. Restless Calderas

Caldera systems are often associated with long episodes of unrest including deformation, but without eruption (Del Gaudio et al., 2010; Lowenstern et al., 2006) and statistically, only 25% of the calderas at which deformation has been observed with InSAR have also erupted (Biggs et al., 2014). Deformation has been previously observed at several of the calderas in the EARS, including Corbetti, Aluto, Tullu Moje, Longonot, Menegai, Paka, and Suswa (Table 1) and in the period 2015–2020, we observed deformation at Corbetti, Tullu Moje, and Suswa.

#### 3.1.1. Corbetti (MER)

Corbetti is a 15-km wide caldera formed during an ignimbrite eruption at 182 ± 28 ka (Hutchison et al., 2016a). Postcaldera eruptions during the Holocene have formed two volcanic centers, Chabbi and Urji (Rapprich et al., 2016). The reconstruction of eruptive history for the last 10 ka suggests a recurrence interval for silicic eruptions of ~900 years with the youngest event occurring between 1.3 and 0.5 ka (Fontijn et al., 2018; Martin-Jones et al., 2017). Corbetti is currently undergoing geothermal exploration and circulation of hydrothermal fluids is associated with shallow seismicity (0–5 km) distributed in two elongated clusters beneath Urji and Chabbi (Lavayssière et al., 2019). The Envisat survey of Biggs et al. (2011) detected ~14 cm of subsidence in 1997–2000, no deformation in 2003–2008. and ~4.2 cm of uplift in 2008–2009 (Table 1). A detailed analysis using ALOS and Envisat data sets from 2007 to 2008 showed minor deformation locally controlled by a E-W cross-cutting structure aligned with the caldera long axis (Lloyd et al., 2018a). Relative uplift of the southern block in June–December 2007 and subsidence in December 2007 to November 2008 was interpreted as pressure changes in a shallow (<1 km) hydrothermal system.

Corbetti is the location of the largest amplitude signal captured by our Sentinel-1 survey. The signal is 15-km wide, with a maximum line-of-sight (LOS) cumulative displacement of 25 cm observed at the center of the caldera (Figure 2a). Lloyd et al. (2018b) combined InSAR data sets from three different satellites (Sentinel-1, ALOS, and COSMO-SkyMed) to produce a decadal time series (October 2007–January 2017) and showed uplift at a constant rate of 5–5.5 cm/yr (Table 1). We extend the Sentinel-1 InSAR time series to 2020, and find that the linear trend remains exceptionally steady at a rate of 4.6 ± 0.1 cm/yr (LOS descending) (Figure 2d), consistent with previous results (Lloyd et al., 2018b). Microgravity measurements taken in 2014–2017 demonstrate that the source of uplift must be magmatic rather than hydrothermal (Gottsmann et al., 2020). Using available constraints on temperature and material properties, Gottsmann et al. (2020) showed that the gravity and deformation measurements for the period 2014–2017 are consistent with the incremental growth of a compressible reservoir within an inelastic medium at ~7-km depth, requiring only modest pressure changes (<10 MPa/yr).

#### 3.1.2. Tullu Moje (MER)

Bora, Bericha, and Tullu Moje are three volcanic centers composed of low-relief pumice domes and ridges (Fontijn et al., 2018). The most recently recorded eruptive activity occurred around 1900 and was associated with the emplacement of obsidian lava flows north of Tullu Moje (Bizouard & Di Paola, 1978). Envisat detected two pulses of uplift in 2004 and 2008–2010 (~2 cm/yr) with intervening subsidence (Biggs et al., 2011) (Table 1). Tullu Moje is a prospect site for geothermal exploitation and a magnetotelluric (MT) survey confirmed the presence of melt and the circulation of hydrothermal fluids below the volcanic area (Samrock et al., 2018). The magmatic system is thought to consist of a mush zone at a depth of <14 km

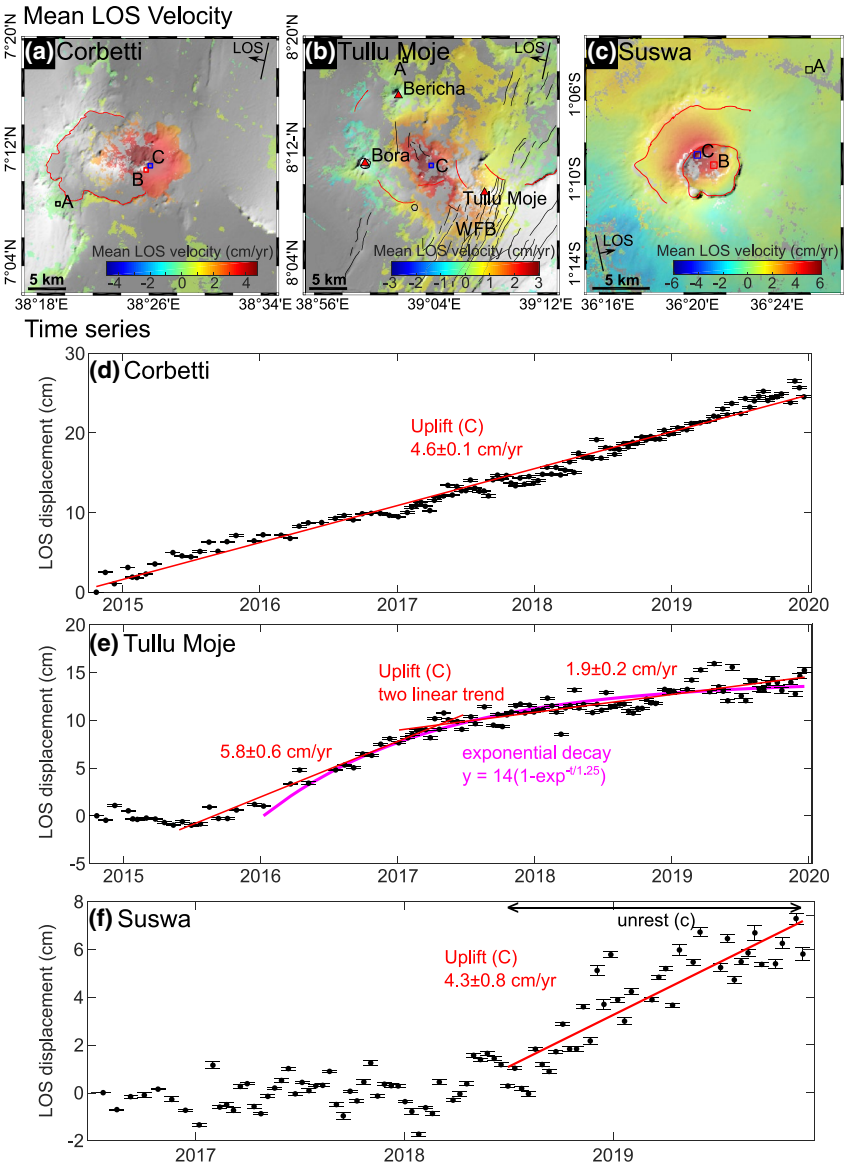


**Figure 2.** Ground uplift signals detected at Corbetti, Tulu Moje, and Suswa volcanoes for the period 2015–2020. (a) Mean LOS velocity at Corbetti. The red line outlines the caldera ring fault structure. (b) Mean LOS velocity at Tullu Moje. The red and black lines show the major faults, including the caldera ring fault and the Wonji Fault Belt (WFB). (c) Mean LOS velocity at Suswa calculated for the unrest period (July 2018 to December 2019). The red line outlines the rim of the two nested calderas. (d) Time series for Corbetti (point C), showing linear uplift causing displacement rate of 4.6 ± 0.1 cm/yr in the LOS. (e) Time series for Tullu Moje (point C), showing exponentially decaying uplift with LOS displacement rates ranging from 5.8 ± 0.6 to 1.9 ± 0.2 cm/yr. (f) Time series for Suswa (point C), showing a new episode of uplift starting in mid-2018 causing displacement rate of 4.3 ± 0.8 cm/yr in the LOS. LOS, line-of-sight.

beneath the rift center connected by a westward-dipping conductive conduit to a shallow reservoir (~4 km) below the volcanic edifice. A resistive body detected at shallow depth (0–3 km) between Tullu Moje and Bora is likely to correspond to a hydrothermal system as its location coincides with an area of vigorous fumarolic activity and hydrothermal alteration. The spatial extent of ground unrest correlates with the location of seismic swarms recorded during a campaign in 2016–2017 (Greenfield et al., 2019b). Although the majority of events are volcano-tectonic, two clusters located below Tullu Moje contained low-frequency waveforms that are likely to be triggered by pulses of hydrothermal fluids ($H_2O/CO_2$) into a fractured region from a shallow magma body located 4–6.5 km below the surface (Greenfield et al., 2019a, 2019b).

The Sentinel-1 survey detected a new pulse of ground deformation between the three volcanic centers—Tullu Moje, Bora, and Bericha—elongated in an NW-SE direction (Figure 2b). The deformation started in early 2016 at a rate of 5.8 ± 0.6 cm/yr (LOS descending), decreasing rapidly with time to an average rate of 1.9 ± 0.2 cm/yr for the period 2017–2020 (Figure 2e—red solid line). The temporal evolution, $U(t)$ can be modeled by an exponential decay function, $U(t) = U_{\infty}(1 - e^{\frac{-t}{\tau}})$, characterizing a hydraulic connection between two magma bodies (Lengliné et al., 2008; Rivalta, 2010) with an asymptotic displacement, $U_{\infty} = 14$ cm and characteristic time $\tau = 1.25$ years (Figure 2e—pink solid line). These observations confirm the episodic behavior of this magmatic system and the exponential decay suggests a migration of fluids between two reservoirs, in agreement with seismic and MT studies (Greenfield et al., 2019a, 2019b; Samrock et al., 2018).

#### 3.1.3. Suswa (Kenya)

Mount Suswa, the southernmost Holocene volcano in the Kenya rift valley, is a large shield edifice (>700 km$^2$) with two nested summit calderas, dominated by phonolitic-to-trachytic lavas and tuffs (White et al., 2012). No eruptions have been dated, but fumaroles are currently observed at the margin of the caldera and the area is a prospect for geothermal exploitation (Simiyu, 2010). An ERS survey of Kenya detected 2–5 cm of subsidence at Suswa between 1997 and 2000 (Biggs et al., 2009a) (Table 1).

The Sentinel-1 survey detected a radially symmetric signal with a radius of 4–5 km. (Figure 2c). The deforming area is offset 1–2 km NW from the center of the summit caldera due to the LOS geometry. The onset of ground deformation started around July 2018 and continued through the year 2019, with a maximum rate of 4.3 ± 0.8 cm/yr (LOS ascending) (Figure 2f). The time series stopped in December 2019 as no data were available for the year 2020. The observations suggest that the deformation is caused by the pressurization of an axisymmetrical source located below the summit crater.

### 3.2. Dike Intrusions

The emplacement of dike intrusions is favored by extensional settings as the minimum compressive stress $\sigma_3$ is subhorizontal. Therefore, dikes are often associated with rift zones at divergent plate boundaries such as Iceland (Gudmundsson, 1995; Hjartardóttir et al., 2012) or on the flank of oceanic volcanoes such as Kilauea (Cervelli et al., 2002; Rubin, 1990). Magma propagation at shallow levels induces strong seismic and geodetic signals. The seismicity captures the dynamic of the intrusion whereas the analysis of ground deformation signals helps to constrain the geometry and the volume change of the intrusion. In the EARS, most intrusive events have been initially detected by the Ethiopian Seismic Stations Network, and subsequently studied using InSAR, including at Ayelu-Amoissa in 2000 (Keir et al., 2011), Dallol in 2004 (Nobile et al., 2012), Dabbahu-Manda-Hararo between 2005 and 2010 (Ayele et al., 2007; Grandin et al., 2010a; Hamling et al., 2009; Wright et al., 2006), Gelai in 2007 (Baer et al., 2008; Biggs et al., 2009b; Calais et al., 2008), Alu-Dalafilla in 2008 (Pagli et al., 2012), and Fentale in 2015 (Temtime et al., 2020) (Table 1). The deformation patterns of dike intrusions are characterized by upward and outward motion either side of the dike and subsidence immediately above it (Rubin, 1992). Dikes along the EARS are preferentially oriented N-S as a result of the rift extension. Because of the inclined LOS, the resulting deformation pattern in an interferogram for an N-S oriented vertical dike is typically asymmetrical with a high magnitude range decrease in the eastern lobe and a small range increase in the western lobe for the descending track (and inversely for the ascending track).

#### 3.2.1. Erta Ale (Afar)

Erta Ale has a persistent lava lake, which has been observed in the south pit of its caldera for at least a century (Oppenheimer & Francis, 1997). Deformation associated with a dike intrusion was detected in 2004–2005 using Envisat InSAR data (Barnie et al., 2016a). The Sentinel-1 survey spans a fissure eruption which started on January 21, 2017, a few days after an overflow of the lava lake. The coeruptive signal during January 2017 shows a complex pattern of deformation with different lobes of negative (range increase) and positive (range decrease) LOS displacement (Figure 3a). Our time series is consistent with previous studies (Moore et al., 2019; Xu et al., 2017, 2020), showing (1) steady preeruptive inflation, (2) rapid deformation during the emplacement of the intrusion, and (3) slow subsidence after the intrusion (Figure 3c).

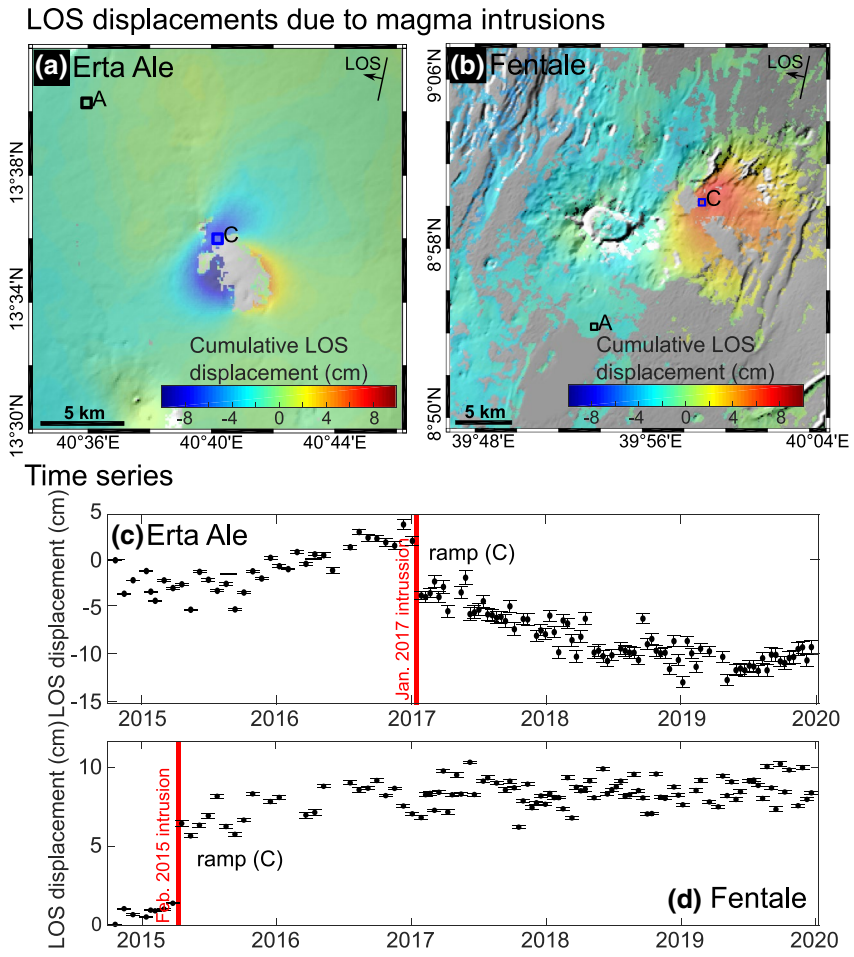


**Figure 3.** Ground deformation signals caused by the emplacement of dike intrusions at (a) Erta Ale (January 2017) and (b) Fentale (February–March 2015) volcanoes. The points A and C correspond to an area without deformation and the maximum displacements, respectively. (c) Time series at Erta Ale (C) showing preeruptive (uplift), coeruptive (ramp), and posteruptive (subsidence) displacements associated with the 2017 eruption. (d) Time series at Fentale (C) showing the ramp displacement associated with the 2015 intrusion.

In detail, the time series for the period 2017–2020 shows a broad region of range increase between the three volcanic centers Erta Ale, Ale Bagu, and Hayli Gubbi (Figure 4), with the highest rates of ∼−7 cm/yr (LOS descending) located inside the 2017–2019 lava flow (Figure 4a—point C1). The spatial distribution of the deformation suggests the superposition of two processes: (i) the depressurization of a magma body causing LOS displacement rate of ∼−4 cm/yr (Figure 4b—point C2) and (ii) the compaction of the lava flow causing LOS displacement rates ranging between −2 and −4 cm/yr depending on the lava thickness (see Section 3.5). Xu et al. (2020) modeled the broad signal with an NE-SW elongated magma body located off-rift between Erta Ale and Ale Bagu. Although the source depths are poorly constrained, they suggest that subsidence is the consequence of magma withdrawal from vertically stacked magma bodies located between 4 and 11 km.

### 3.2.2. Fentale (MER)

Seismicity and deformation were detected to the northeast of Fentale volcano during February–March 2015. The descending track of Sentinel-1 data shows a large range decrease with a maximum LOS displacement of 7 cm located northeast of the edifice (Figures 3b and 3d). Combining Sentinel-1 and COSMO-SkyMed data from ascending and descending tracks, Temtime et al. (2020) modeled a dike intrusion at depths of 5.4–8 km with a total volume change of $33 \pm 0.6 \times 10^6$ m$^3$. The dike emplacement took nearly 3 months, much longer than dike intrusions in the Afar which emplaced in time scales ranging from hours to days (Ayele

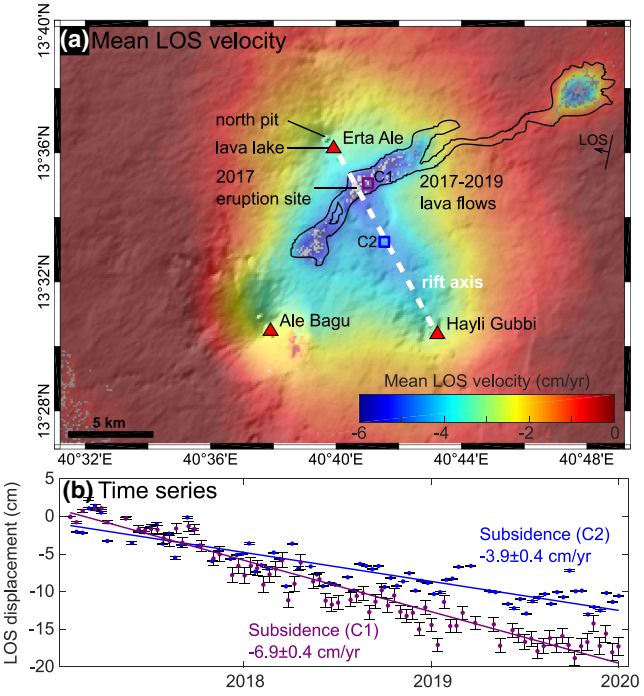


**Figure 4.** Ground deformation signals detected after the 2017 Erta Ale intrusion. (a) Mean LOS velocity calculated for the period between January 22, 2017 and December 31, 2019, showing two superposed signals: (i) subsidence caused by the compaction of the 2017–2019 lava field (black solid line) and (ii) broad subsidence along the rift axis (white dashed line) related to the contraction of a magma body. (b) Time series showing LOS displacement rates of −6.9 ± 0.4 and −3.9 ± 0.4 cm/yr for the superposed signals (C1) and the contraction of the magma body (C2), respectively. LOS, line-of-sight.

et al., 2009; Barnie et al., 2016b; Grandin et al., 2011; Keir et al., 2009), suggesting a higher viscosity magma was involved (Temtime et al., 2020).

### 3.3. Deformation Following Eruptions and Intrusions

Ground deformation can be recorded months to years after an eruption or intrusion, with examples of both uplift and subsidence (Delgado et al., 2018; Hamlyn et al., 2018). Two distinct mechanisms have been proposed to explain exponentially decaying uplift: (i) magma recharge of a shallow reservoir from a deep reservoir (Le Mével et al., 2016; Lengliné et al., 2008) or (ii) viscoelastic relaxation of the host rocks around the reservoir (Newman et al., 2001; Segall, 2016). Interestingly, the latter process can induce uplift without any recharge for incompressible magmas embedded in a small viscoelastic aureole associated with large relaxation time and/or small recharge time (Segall, 2016). For compressible magmas and without recharge, viscoelastic relaxation would cause slow subsidence as illustrated by the case of the Nabro 2011 eruption (Hamlyn et al., 2018). Posteruptive subsidence can also be caused by a volume decrease in the magma reservoir due to cooling and crystallization (Caricchi et al., 2014; Poland et al., 2006) or pressure decreases in the hydrothermal system (Hamling et al., 2016; Narita & Murakami, 2018).

#### 3.3.1. Dabbahu-Manda-Hararo Volcanic System (Afar)

In September 2005, a major volcano-tectonic event occurred in the Dabbahu-Manda-Hararo magmatic segment causing deformation, persistent seismic swarms, and a minor eruption at the Dabbahu-Gabho volcanic complex (Ayele et al., 2007; Ebinger et al., 2008; Yirgu et al., 2006). Envisat observations showed a 2–3-km wide central area of subsidence (up to 2 m) associated with vertical (up to 1.5 m) and horizontal motion (up to 2 m) on either side (Grandin et al., 2009; Wright et al., 2006). By modeling the InSAR data, the volume of the dike was found to be in the range of 1.5–2.5 km$^3$ (Ayele et al., 2007; Grandin et al., 2009; Wright et al., 2006). Subsidence signals related to small shallow magma reservoirs below Dabbahu and Gabho volcanic centers were detected (Grandin et al., 2009; Wright et al., 2006), but as the volume change of these shallow sources only corresponds to a small fraction (~30%) of the total intruded volume, the intrusions are thought to originate from a midsegment magma reservoir located at >10 km below the Ado'Ale Volcanic Complex (AVC) (Ayele et al., 2009; Ebinger et al., 2008; Grandin et al., 2010b; Keir et al., 2009). This episode was followed by a series of 13 smaller dike intrusions (0.04–0.2 km$^3$) during the period 2006–2010 (Barnie et al., 2016b; Grandin et al., 2010a, 2010b; Hamling et al., 2009). Postdiking ground deformation signals (2005–2010), with vertical and rift perpendicular rates of up to 24 and 18 cm/yr, respectively, have been interpreted as either the viscoelastic relaxation of the upper mantle (Hamling et al., 2014; Nooner et al., 2009) or the redistribution of magma between hydraulically connected reservoirs (Grandin et al., 2010b; Pagli et al., 2014).

The Sentinel-1 survey covers a period 10–15 years after the major 2005 dike intrusion and starts 5 years after the last small dike. We detect a broad deformation signal (~2,600 km$^2$) along the rift segment between Dabbahu and Manda-Hararo (Figure 5a). The ground deformation is greatest on the eastern side of the rift (up to 40 km from the rift axis) due to the descending line-of-sight. The highest rates of displacement are detected near the two volcanic centers Dabbahu and Ado'Ale Volcanic Complex (AVC) with values of 3.9 ± 0.3 and 3.0 ± 0.3 cm/yr, respectively (Figure 5c). The pattern of deformation is similar to that of 2006–2010 (see Figure 4 in Hamling et al. (2014)), but the mean LOS velocity has decreased by a factor of 5, from ~20 cm/yr (2006–2010) to ~4 cm/yr (2015–2020). Our Sentinel-1 InSAR confirms a rapid decay of the rates of LOS displacement since the diking event, which could be caused by either (i) the progressive repressurization of an elastic reservoir due to magma recharge from a deep source (Grandin et al., 2010b; Pagli et al., 2014) or (ii) the continuous viscous relaxation of the upper mantle without magma recharge (Hamling et al., 2014; Nooner et al., 2009).

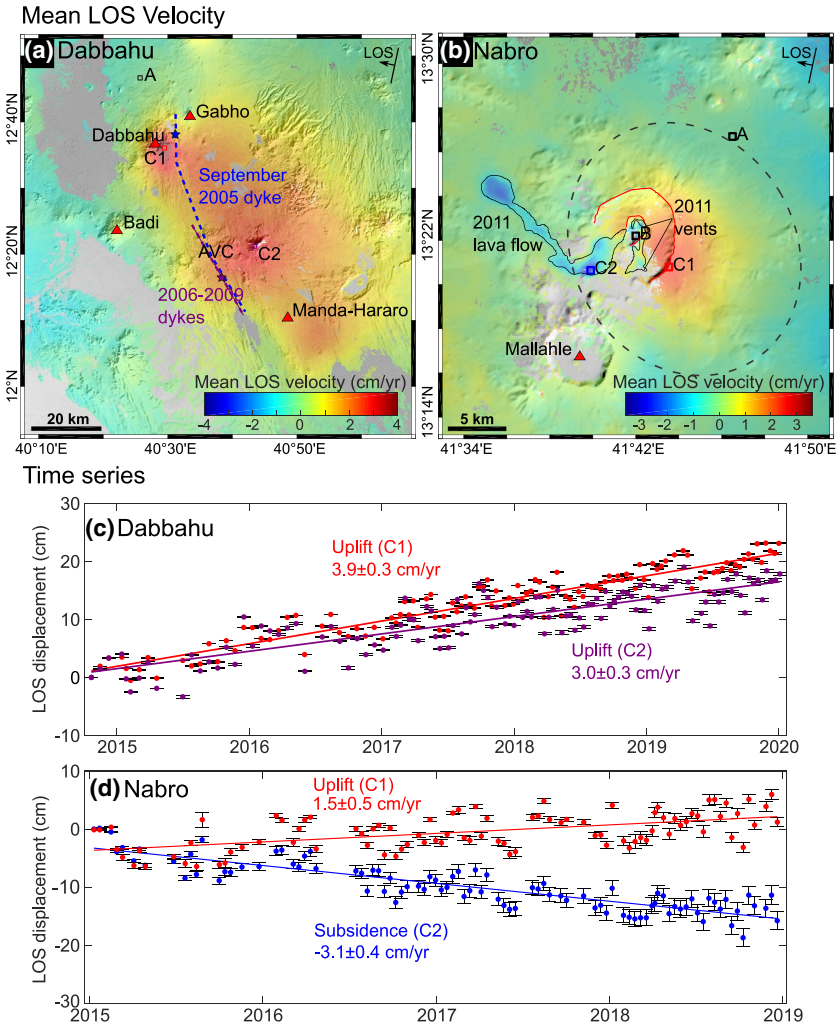


**Figure 5.** Ground deformation signals detected at the Dabbahu-Manda-Hararo rift segment for the period 2015–2020 and Nabro volcano for the period 2015–2019. (a) Mean LOS velocity at the Dabbahu-Manda-Hararo rift segment. Red triangles indicate the major volcanic centers (AVC, Ado'Ale Volcanic Complex). Blue and purple dashed lines indicate the trace of the September 2005 diking event and the 2006–2009 dike intrusions, respectively, and the stars show the location of the corresponding eruptions (Grandin et al., 2010a; Wright et al., 2006). The points C1 and C2 correspond to two areas of maximum uplift located at the stratovolcano Dabbahu (C1) and the Ado'Ale Volcanic Complex (C2). (b) Mean LOS velocity at Nabro volcano. Dashed line shows the extend of the 2011 subsidence signal for comparison (Hamling et al., 2014). Black and red solid lines outline the 2011 lava flow (Goitom et al., 2015) and the caldera ring, respectively. The points C1 and C2 correspond to the areas of maximum uplift and maximum subsidence, respectively. (c) Time series of the signal located at Dabbahu-Manda-Hararo rift segment, showing LOS displacements rates of 3.9 ± 0.3 and 3.0 ± 0.3 cm/yr for Dabbahu (C1) and AVC (C2), respectively. (d) Time series at Nabro, showing LOS displacement rates of 1.5 ± 0.5 cm/yr for the uplift signal (C1) and −3.1 ± 0.4 cm/yr for the subsidence signal (C2). LOS, line-of-sight.

### 3.3.2. Nabro (Afar)

Nabro is the highest stratovolcano in the Danakil depression and is composed of trachytic flows and pyroclastic deposits (Wiart & Oppenheimer, 2005). The summit is truncated by two nested calderas of 5-km and 8-km radius. An earthquake swarm was recorded on the evening of June 12, 2011, followed by the eruption (between 20:27 and 20:45 UTC) causing the emission of a plume into the lower stratosphere and the emplacement of a lava flow (Goitom et al., 2015; Clarisse et al., 2014; Figure 5b). Coeruptive deformation with maximum LOS displacements of −40 cm was modeled with the interaction between a shallow dike and a normal fault (Goitom et al., 2015). Later, a 12-km wide posteruptive subsidence signal with an exponential

decay rate was detected between July 2011 and October 2012, and interpreted as the viscoelastic relaxation of a spherical source located at 6–7-km depth (Hamlyn et al., 2018).

The Sentinel-1 survey shows two superposed signals: a localized LOS range increase on the western flank associated with the 2011 lava flows (see Section 3.5) and a radially symmetric range decrease of ∼5 km located on the eastern side of the edifice (Figure 5b). This signal is offset from the center due to the descending line-of-sight. The location of this signal is similar to that of the posteruptive subsidence signal detected by Hamling et al. (2014) but the extent is smaller (Figure 5b—dashed line). At 1.5 ± 0.5 cm/yr, the displacement rate remains small and difficult to distinguish from noise. These observations show that Nabro experienced a transition from posteruptive subsidence to uplift between 2012 and 2014, possibly due to the fresh influx of magma.

#### 3.3.3. Alu-Dalafilla (Afar)

Alu-Dalafilla is composed of a basaltic cone (Alu) and a silicic stratovolcano (Dalafilla). The first historical eruption occurred on November 2008, when fissures opened between the two edifices and produced lava flows which traveled up to 9 km NE of the vent (Pagli et al., 2012). Pagli et al. (2012) used ALOS and Envisat SAR data to detect deformation signals associated with: (i) preeruptive uplift caused by the pressurization of a shallow sill; (ii) coeruptive subsidence due to magma withdrawal during the dike intrusion; (iii) posteruptive uplift related to the rapid replenishment of the reservoir (30% of the coeruptive volume was recovered by September 2010). The posteruptive uplift signal was composed of two independent lobes centered on Alu and Alu-South, which suggests partitioning of the magma storage.

The Sentinel-1 survey detected two lobes of range increase (Figures 1d and 6a) at rates of −1.6 ± 0.2 and −1.2 ± 0.2 cm/yr (LOS descending) for Alu and Alu-South, respectively (Figure 6c). The pattern of deformation is similar to the 2008 posteruptive signal reported by Pagli et al. (2012), but the sign of motion reversed from rapid uplift (10–20 cm/yr) during 2008–2010 to slow subsidence (1–2 cm/yr) during 2015–2020 (Figure 6c), which suggests pulses of activity.

#### 3.3.4. Dallol (Afar)

The Dallol rift segment is located in the Danakil depression (∼120 m b.s.l) and composed of a large network of salt mounds and ridges that formed at least ∼32,000 years ago where the area was covered by the sea (Bonatti et al., 1971). Dallol volcano is a small mound (∼2-km wide and 30–40-m high) associated with an intense hydrogeothermal activity (Carniel et al., 2010; López-García et al., 2020). The only reported activity was a phreatic eruption in 1926 that produced a 30-m diameter crater (Global Volcanism Program, 2013).

Envisat observations in 2014 showed a complex pattern of ground deformation with (i) a range increase (−30 cm) extending 9 km south from Dallol edifice in the rift direction, (ii) a range decrease in the eastern flank (∼+17 cm), (iii) a range increase in the western flank (∼−17 cm), and (iv) a circular area of range increase (∼−12 cm) centered on Dallol edifice (Nobile et al., 2012). The deformation signals were modeled by the combination of three sources: a 0.06 $km^3$ subvertical NW-SE trending dike south of Dallol, a deflating Mogi source between 1.5 and 3.3 km of depth below Dallol, and a normal fault on the western side of the dike intrusion (Nobile et al., 2012).

The Sentinel-1 survey detected a radially symmetric signal (∼1-km radius) of range increase centered on the volcanic edifice between 2015 and 2020 (Figure 6b). The time series shows a linear trend at a maximum rate of −3.3 ± 0.1 cm/yr (LOS descending) implying a continuous process (Figure 6d). The signal is <2.5 km across suggesting it is associated with the decrease in volume change of a shallow reservoir. Our 5-year observations confirm the presence of a deflating source below Dallol, which is in accordance with models proposed for the 2004 diking event.

### 3.4. Shallow Subsidence and Seasonal Signals Caused by Pore-Pressure Changes

Deformations signals have been observed at many geothermal fields worldwide with rates of displacements ranging from few cm/yr to 50 cm/yr (Allis, 2000; Carnec & Fabriol, 1999; Massonnet et al., 1997; Mossop & Segall, 1997). Subsidence at geothermal fields can be related to the depletion of fluid storage (e.g.,

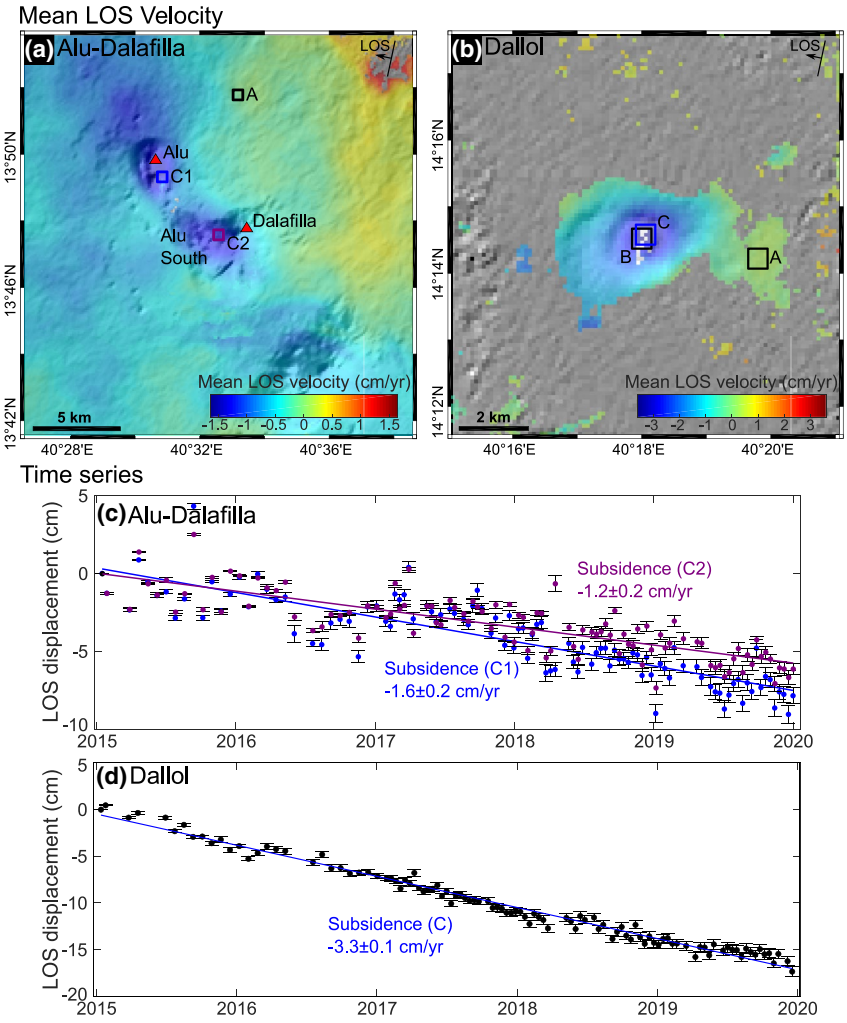


**Figure 6.** Ground deformation signals detected at Alu-Dalafilla and Dallol volcanoes for the period 2015–2020. (a) Mean LOS velocity at Alu-Dalafilla. Red triangles indicate the main volcanic centers. (b) Mean LOS velocity at Dallol. (c) Time series at Alu-Dalafilla showing displacement rates of −1.6 ± 0.2 and −1.2 ± 0.2 cm/yr in the LOS for Alu (C1) and Alu-South (C2), respectively. (d) Time series at the center of Dallol volcano (C) showing linear subsidence causing a displacement rate of −3.3 ± 0.1 cm/yr in the LOS. LOS, line-of-sight.

extraction ≫ injection), the compaction of host rocks caused by the decrease of pore pressure, the thermal contraction of the host rocks or strain release on nearby faults (Araya & Biggs, 2020; Barbour et al., 2016; Fialko & Simons, 2000; Narasimhan & Goyal, 1984; Sarychikhina et al., 2011).

The East African Rift is a major target for geothermal exploration (Omenda & Teklemariam, 2010; Simiyu, 2010). Kenya is the largest producer of geothermal energy in Africa, with five power plants operated at the Olkaria geothermal field, one under construction at Menengai, and several additional prospect areas (Eburru, Suswa, Silali, Longonot, Akiira, and Barrier) (Mangi, 2018). In Ethiopia, Aluto-Langano is the only geothermal field exploited so far, but 22 prospect sites have been identified and five of them (Tendaho, Abaya, Tulu-Moye, Corbetti, Dofan Fantale) have been selected for future geothermal development plans (Kebede, 2016).

In the EARS, the circulation of hydrothermal fluids and $CO_2$ surface degassing is controlled by rift-related extensional faults as well as local volcanic structures (Hutchison et al., 2015; Lee et al., 2016; Robertson et al., 2016). Under some conditions, the pore-fluid pressure changes related to these shallow

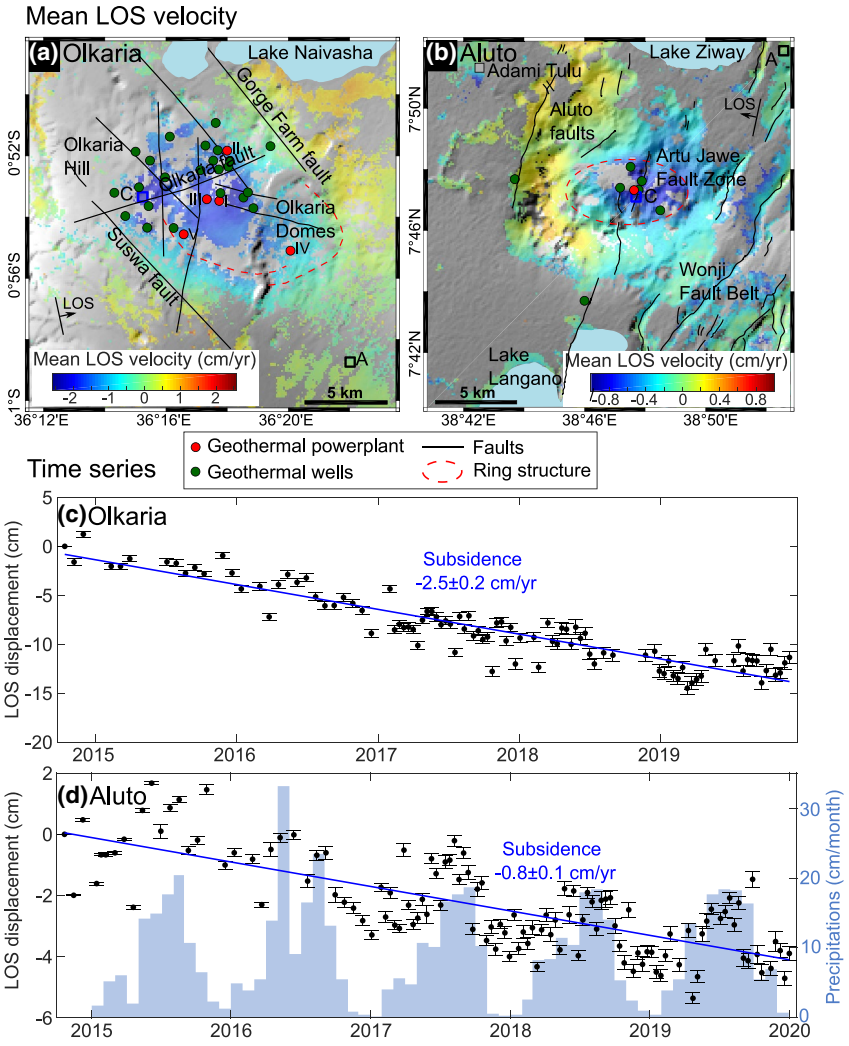


**Figure 7.** Ground deformation signals detected at Olkaria (Kenya) and Aluto (MER) volcanoes for the period 2015–2020. (a) Mean LOS velocity at the geothermal field Olkaria. Red circles indicate the five powerplants (from I to V) and the green circles correspond to the main geothermal wells (Omenda, 1998). The solid black lines and the dashed red lines show the major faults and the ring structure, respectively (Clarke et al., 1990). (b) Mean LOS velocity at Aluto volcano. The red circle indicates the geothermal powerplant and the green circles correspond to the geothermal wells (Wilks et al., 2017). Solid lines show the fault system: the border faults (Agostini et al., 2011), the Aluto faults and the Artu Jawe fault (Kebede et al., 1985). The dashed red ellipse indicates the ring structure of the caldera (Hutchison et al., 2015). (c) Time series at Olkaria complex (C) showing a long-duration subsidence causing displacement rate of −2.5 ± 0.2 cm/yr in the LOS. (d) Time series at Aluto (C) showing the superposition of a seasonal trend and a long-duration slow subsidence (displacement rate of −0.8 ± 0.1 cm/yr in the LOS). The blue histogram shows the daily precipitation in the area. LOS, line-of-sight.

magmatic/hydrothermal systems are sufficient to reactivate existing structures causing seismic swarms and ground deformation signals that are typically fault bounded (Biggs et al., 2013; Doubre & Peltzer, 2007).

### 3.4.1. Olkaria (Kenya Rift)

Olkaria is a Holocene volcanic complex and is the most productive geothermal field in Africa. In 1981, the Kenya Electricity Generating Company (KenGen) began operating the first geothermal power plant in Africa. The plant has expanded to five operational stations (Figure 7a) with a total production of ~690 MW in 2020 (Mangi, 2018), However, previous Envisat surveys of the Olkaria geothermal field spanning 2003–2010 did not show any clear evidence of ground deformation related to geothermal exploitation (Biggs et al., 2009a, 2016; Koros & Agustin, 2017).

The Sentinel-1 survey identifies the first significant deformation at Olkaria: a 10-km wide area of range increase (Figure 7a). The orientation and the extent of the signal are controlled by the NW-SE rift fault system (Omenda, 1998) (e.g., Suswa and Gorge Farm faults) and the caldera ring fault. The displacement rate reaches −2.5 ± 0.2 cm/yr (LOS ascending) for the period 2015–2020 (Figure 7b). During 2014–2015, KenGen completed a large 280-MW expansion project that doubled the production rate (Rotich, 2016), which may have caused subsidence to begin.

#### 3.4.2. Aluto (MER)

Aluto is a wide caldera (~42 $km^2$) formed during two successive large-volume ignimbrite eruptions at 316 ± 19 and 306 ± 12 ka (Hutchison et al., 2016b). The reconstruction of the postcaldera eruptive history (e.g., from 55 ± 19 to 0.40 ± 0.05 ka) suggested a time of recurrence of silicic eruptions of ~1,000 years, which is similar to that of Corbetti volcano (Hutchison et al., 2016a, 2016b). However, complementary tephra-stratigraphy studies of the last 12,000 years recorded 25 eruptions during three pulses of activity at ~3, 6.5, and 11 ka, which indicates a higher rate of recurrence during the Holocene with 2–3 explosive eruptions per millennium (Fontijn et al., 2018; McNamara et al., 2018). The Aluto-Langano power plant has been operating since 1998, but at a low rate of production (7.2 MW) (Kebede, 2016).

Envisat detected two rapid pulses of uplift in 2004 (10–15 cm) and 2008 (8–10 cm) each followed by slow subsidence (~-5 cm) (Biggs et al., 2011; Hutchison et al., 2016c). Uplift is thought to be caused by episodic deep magmatic injections whereas subsidence is caused by the depressurization of the hydrothermal reservoir due to the cooling or loss of fluids through shallow structures such as the Artu Jawe Fault Zone (AJFZ) and ring faults (Braddock et al., 2017; Hutchison et al., 2015). A seismic survey during 2012–2014 found high levels of seismicity above sea level with a *b*-value consistent with the circulation of hydrothermal fluids and a deeper zone of seismicity (2–9 km) associated with a zone of magma storage (Wilks et al., 2017, 2020). The seismicity in the hydrothermal reservoir is seasonal, with the major peak of seismicity 2–3 months after the rainy season, coincident with the high stand of nearby lakes and maximum subsidence recorded by GPS, indicating that it is driven by surface loading rather than a pore-pressure changes in the hydrothermal system (Birhanu et al., 2018). In addition, Nowacki et al. (2018) used shear-wave splitting to confirm that the circulation of fluids is confined within the edifice (within the top 3 km b.s.l.) and occurred through two sets of cracks (e.g., aligned to E-W extension and parallel to Wonji Fault Belt).

The Sentinel-1 survey detected an ongoing range increase signal inside the caldera at the small rate of −0.8 ± 0.1 cm/yr (LOS descending), with a similar spatial pattern to previous studies (Biggs et al., 2011; Hutchison et al., 2016c) (Figure 7b). The higher temporal resolution following the launch of Sentinel-1B in 2016 shows that there is a clear seasonal signal with an amplitude of 2–3 cm superimposed on the long-term trend (Figure 7d), consistent with the GPS observations of Birhanu et al. (2018). However, when compared to monthly precipitation records from Harris et al. (2020), we find that the peak of subsidence occurred during the driest months (November to January) and the peak of uplift during the wettest months (July to September) (Figure 7d), suggesting that the processes driving seasonal deformation (e.g., precipitations and lake loading) vary in time and space.

#### 3.4.3. Haledebi (MER)

Haledebi is a local village located 10 km south of Hertali volcano. Although it is not listed as a Holocene volcano, fresh-looking lava flows are visible on optical imagery and Biggs et al. (2011) detected an asymmetrical deformation pattern with uplift (~4 cm) from June to December 2007 followed by continuous subsidence (~−5 cm) until mid-2010 (Table 1).

The Sentinel-1 survey detected a sharp-edged pattern of deformation (~37.5 $km^2$) aligned with the rift (Figures 8a and 8b), which is very similar to the pattern detected during 2007–2010 (Biggs et al., 2011). Because the Sentinel-1 data set has higher temporal resolution (12 days since 2017) than previous Envisat/ERS data set, we are now better able to constrain the timing of the cycles of deformation. The time series shows rapid LOS range decrease (+9.5 ± 2.6 and +8.5 ± 2.8 cm/yr) from June to December followed by slow LOS range

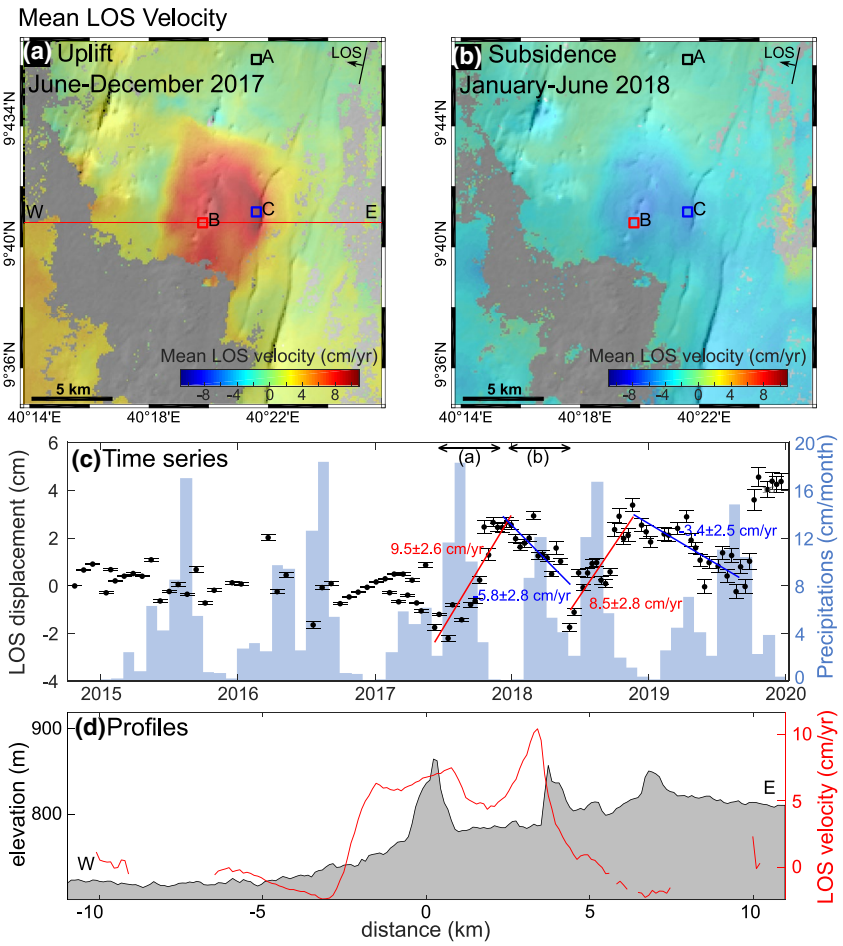


**Figure 8.** Ground deformation signals detected at Haledebi for the period 2015–2020. Mean LOS velocity showing (a) uplift between June and December 2017 and (b) subsidence between January and June 2018. The points A, B, and C correspond to an area without deformation, the center of the volcano and the area of maximum displacements, respectively. (c) Time series at Haledebi (C) showing successive phases of uplift (displacement rates of 8.5–9.5 cm/yr in the LOS) and subsidence (displacement rates of 3.4–5.8 cm/yr in the LOS). The blue histogram shows the daily precipitation in the area. (d) E-W profile of the mean LOS velocity of the uplift signal (red) showed in panel (a) with the background shaded area corresponding to the topography. LOS, line-of-sight.

increase (−5.8 ± 2.8 and −3.4 ± 2.5 cm/yr) between January and June (Figure 8c). Monthly precipitation shows a bimodal distribution with small peaks around March to May and high peaks corresponding to the rainy season between July and September (Figure 8c) (Harris et al., 2020). The rainy season is correlated with the deformation with a time-lag of about 3 months between the peaks of precipitations and the peaks of LOS displacements. In addition, we notice that high strain is localized near a fault scarp on the eastern margin (Figure 8d), which indicates that such ground deformation could be partly accommodated by the rift faults.

Although this is a volcanic area, it is not clear that the deformation is directly related to magmatic activity. Pore-pressure changes along local tectonic features could explain the cycle of ground deformation: (i) water discharge during the rainy season causes an increase in pore-pressure resulting in rapid uplift; (ii) during the dry season, pore-pressure decreases inducing compaction of the host rock cause small subsidence.

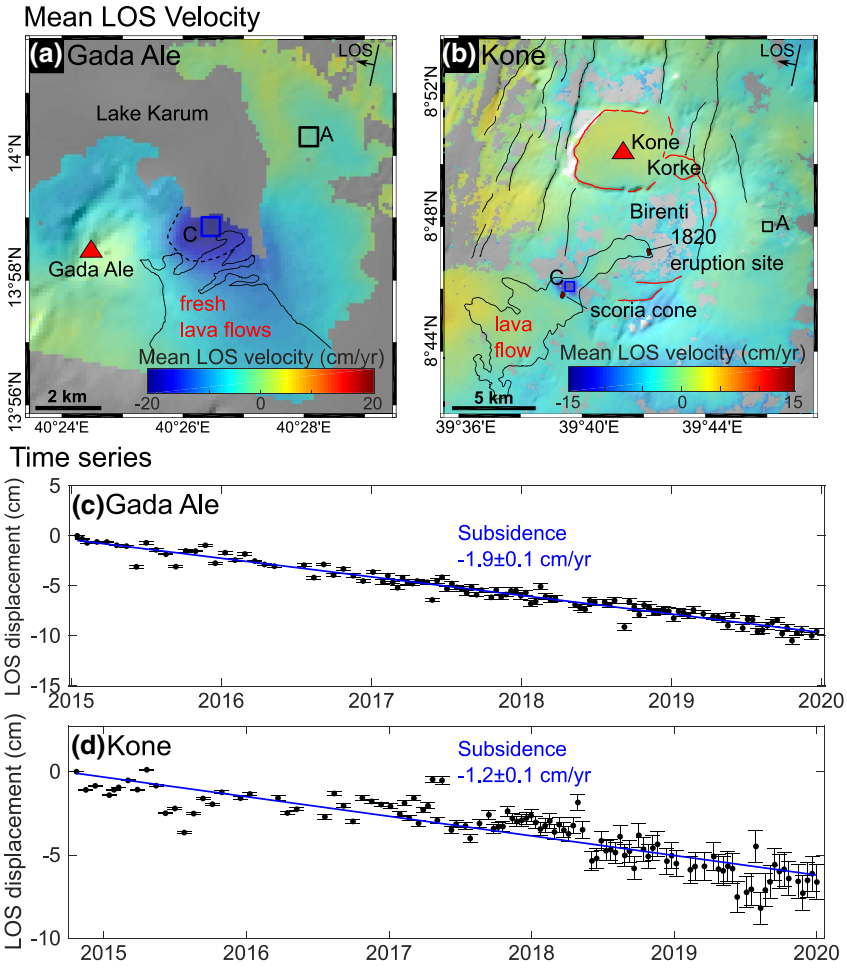


**Figure 9.** Ground deformation signals detected at Gada Ale and Kone volcanoes for the period 2015–2020. (a) Mean LOS velocity at Gada Ale showing a ground subsidence signal at the edge of Lake Karum. Black solid line shows the extend of the fresh lava flows. Dashed line indicates the extend of the signal detected during 1993–1996 by Amelung et al. (2000). (b) Mean LOS velocity at Kone showing a small subsidence signal on the 1820 lava flow (black outline). Black and red lines correspond to the major faults and the caldera ring structures (Rampey et al., 2010). We indicate the eruption site, the scoria cones, and the flow area of the 1820 eruption. (c) Time series at Gada Ale (C) showing long-term linear subsidence causing a displacement rate of −1.9 ± 0.1 cm/yr in the LOS. (d) Time series at Kone (C) showing subsidence causing a displacement rate of −1.2 ± 0.1 cm/yr in the LOS. LOS, line-of-sight.

### 3.4.4. Gada Ale (Afar)

Gada Ale is a stratovolcano formed of successive lava flows and hyaloclastites. Although there are no historical records of eruptive activity, eruptive fissures on the SE flank associated with cinder cones and fresh lava flows may suggest an activity during the Holocene (Global Volcanism Program, 2013). An asymmetric subsidence signal of around 12 cm was detected between 1993 and 1996 using a single pair of ERS-1 image and modeled with the combination of the contraction of a magma body and normal faulting (Amelung et al., 2000).

The Sentinel-1 survey detected a range increase at a constant rate of −1.9 ± 0.1 cm/yr (LOS descending) for the period 2015–2020 in the same area and pattern as the signal from 1993–1996 (Amelung et al., 2000) (Figures 1c, 9a and 9c). The similarity in pattern implies that the same source was active in 1993–1996 and 2015–2020, but there have been no observations of deformation during the 30-year period between, even in the well-studied Envisat era (Pagli et al., 2014). This suggests that either that the mechanism is not persistent over a long time scale or that the rate of displacements was too small to be detected. The deforming area is offset 3–4 km east of the edifice and its extent does not correspond to the location of the most recent lava

flows (Figure 9a—solid line). Intermittent interaction between fluids and local faults at the border of Lake Kurum is one possible mechanism to explain the spatiotemporal characteristics of the signal.

### 3.5. Long-Term Subsidence due to Lava Flow Compaction

Lava flow subsidence has been observed at many volcanoes after effusive eruptions, as compiled by Ebmeier et al. (2012). The subsidence signal is the result of multiple mechanisms with different wavelengths and time scales, often working in concert: (i) the deflection of the flow substrate in response to surface loading, (ii) the thermal contraction of the lava due to cooling, and (iii) the compaction of vesicles and void space. The subsidence rate observed using InSAR spans 2 order of magnitude from 0.6 to 83 cm/yr (Ebmeier et al., 2012), depending on the thickness of the lava and the time since emplacement (Stevens et al., 2001).

#### 3.5.1. Nabro (Afar)

In addition to the uplift signal discussed in Section 3.3.2, we detect range increases located inside the 2011 lava field at Nabro, 4–8 years after emplacement (Figure 5b). The highest rate of LOS displacements ($-3.1 \pm 0.4$ cm/yr) is located in areas where the lava has ponded, close to the vent and at the tip of the flow (Figure 5d—point C2). Subsidence rates observed at Nabro are in agreement with the compaction rates of 2.2–3.5 cm/yr deduced for the 1986–1987 and 1989 lava flows at Etna after 3–4 years of emplacement (Briole et al., 1997) suggesting a maximum thickness of about 10 m, which is consistent with the 5–10 m observed at the flow margins after the 2011 eruption (Hamlyn et al., 2014).

#### 3.5.2. Kone Volcanic Complex (MER)

The Kone volcanic complex is composed of a series of nested silicic calderas (Birenti, Kone, and Korke) accompanied by welded ignimbrite sheets that formed during large explosive eruptions between 320 and 170 ka (Rampey et al., 2010). The only Holocene eruption recorded was an effusive event in 1810–1830, which produced basaltic lava flows in the southern of Kone caldera (Fontijn et al., 2018; Harris, 1844) (Figure 9b).

The Sentinel-1 survey detected a small region of range increase (<1 $km^2$) on the most recent lava field close to a small scoria cone formed during the 1820 eruption (Figure 9b). The maximum LOS rate of displacement is small at $-1.2 \pm 0.1$ cm/yr (Figure 9d). From our knowledge, no ground deformation signal was reported at Kone during the ERS/ENVISAT era (Biggs et al., 2009a). However, previous sensors had a much lower temporal resolution and the resulting data were noisier. It could be that either (i) the mechanism is not long-lasting or (ii) previously, the data were too sparse to detect displacement of this kind. From the characteristics of the signal (e.g., wavelength, location, duration), we propose that the subsidence signal is the result of contraction, compaction or loading of 1820 volcanic products. Given the 200-year period since eruption, this is one of the longest-lasting lava flow subsidence signals yet detected.

## 4. Discussion

### 4.1. Spatial and Temporal Characteristics of Volcanic Deformation in the EARS

Here, we report on 18 ground deformation signals detected at 14 active volcanoes along the EARS. Our analysis shows that these are associated with a variety of processes including: (1) restless calderas, (2) dike intrusions, (3) deformation following eruption or intrusion, (4) pore-pressure changes, and (5) lava flow subsidence. As a result, there is a large diversity in the spatial and temporal characteristics of the deformation signals, depending on the process involved. The area of deformation spans >3 order of magnitude from <1 $km^2$ for the subsidence signal at Kone to 2,600 $km^2$ for the uplift signal of the Dabbahu-Manda-Hararo magmatic system (Table 2). The deformation occurs on different time scales, with rapid deformation (weeks to months) during the emplacement of magma intrusions (Erta Ale and Fentale) and long-lived deformation (>5 years) associated with lava flow compaction (Nabro) or at restless calderas (Corbetti). Interestingly, the period of deformation exceeds the 5-year period of our Sentinel-1 survey for >60% of the

**Table 2**
*Characteristics of the Ground Deformation Signals Detected During Our 2015–2020 Sentinel-1 InSAR Survey*

| Volcano | Area (km$^2$) | Velocity (cm/yr) | Duration (year) | Trend | Offset (km) |
|---|---|---|---|---|---|
| Alu-Dalafilla | 25 | −1.2 − 1.6 | >5 | Linear | 0 |
| Dabbahu-Hararo | 2,600 | 3.9 | >5 | Linear | 0 |
| Dallol | 2.5 | −3.3 | >5 | Linear | 0 |
| Erta Ale[a] | 32 | +3.7 | >2 | Linear | 0 |
| Erta Ale[b] | 37 | −200 + 200 | <0.03 | Ramp | 0 |
| Erta Ale[c] | 216 | −3.9 | >5 | Linear | 0 |
| Erta Ale[d] | 30 | ∼−3 | >5 | Linear | 0 |
| Gada Ale | 9 | −1.9 | >5 | Linear | 3.5 |
| Nabro[e] | 50 | +1.5 | >5 | Linear | 0 |
| Nabro[f] | 20 | −3.1 | >5 | Linear | 0 |
| Aluto | 20 | −0.8 | >5 | Seasonal/linear | 0 |
| Corbetti | 163 | +4.6 | >5 | Linear | 0 |
| Fentale | 70 | +53 | <0.1 | Ramp | 6.3 |
| Haledebi | 64 | +8.5/+9.5 − 3.4/−5.8 | 0.5 | Cycle | 3.3 |
| Kone | <1 | −1.2 | >3 | Linear | 8.5 |
| Tullu Moje | 100 | +5.8 + 1.9 | >5 | Exponential | 7.8 |
| Olkaria | 114 | −2.5 | >5 | Linear | 0 |
| Suswa | 56 | +4.3 | >2 | Linear | 0 |

[a]Preeruptive inflation. [b]Coeruptive intrusion. [c]Posteruptive deflation. [d]Lava flow subsidence. [e]Reservoir inflation. [f]Lava flow subsidence.

signals detected, which emphasizes the need for producing long-duration time series (decades) to better characterize the dynamics of these systems.

In Afar, we detected deformation at 6 of the 30 Holocene volcanoes (Figure 10a), all six of which had also been deforming during earlier studies (Table 1). Most of the deformation signals (5/6) are associated with

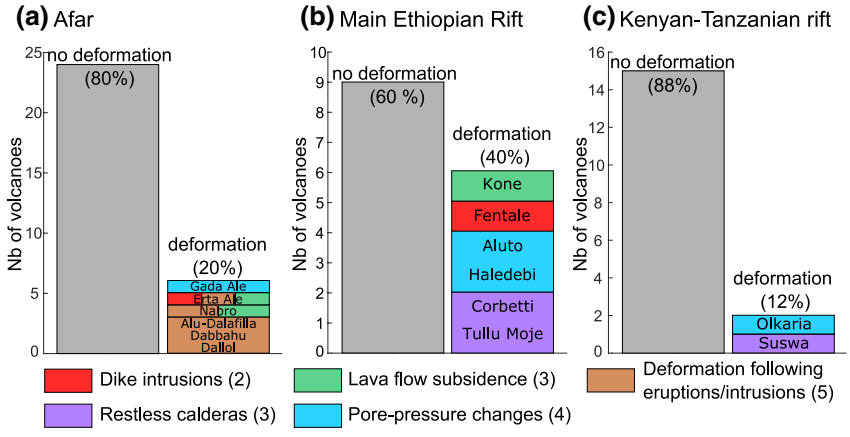


**Figure 10.** Proportion of nondeformed and deformed volcanoes inferred from our 2015–2020 Sentinel-1 survey for each section of the EARS: (a) Afar, (b) Main Ethiopian Rift (MER), and (c) Kenyan-Tanzanian rift. Volcanoes with multiple ground deformation signals are counted once (e.g., Erta Ale and Nabro). Colors refer to the five classes of deformation reported in Section 3: uplift of restless calderas, dike intrusions, deformation following eruptions and intrusions, subsidence and seasonal signals associated with pore-pressure changes, and lava flow subsidence. The number corresponds to the total number of cases per class.

shallow magmatic activity such as the emplacement of dike intrusions (Erta Ale), the reequilibration of magmatic systems following eruptions/intrusions (Erta Ale, Nabro, Alu-Dallafila, Dabbahu-Manda-Hararo, and Dallol) and the compaction of lava flows (Erta Ale, Nabro) (Figure 10a). Continuous uplift lasting the entire 5-year period (2015–2020) was detected at Dabbahu-Manda-Hararo and Nabro and both these volcanoes have experienced recent eruptive activity, with dike intrusions and minor fissure eruptions at Dabbahu in 2005–2010 and an explosive eruption in 2011 at Nabro. The mechanisms of posteruption deformation are complex and uplift could be the result of the repressurization of the magmatic system and/or viscous relaxation (Segall, 2016). Additional data sets such as repeated gravity surveys or continuous gas monitoring will be required to discriminate between the two processes (Henderson et al., 2017). We do not detect any deformation for the period 2015–2020 at two other centers having records of unrest (Table 1): Ayelu (dike intrusion) and Tendaho (geothermal). This indicates that these signals were associated with short-lived events rather than continuous processes.

In the Main Ethiopian Rift, we detect deformation at 6 of the 15 volcanic centers, mostly associated with the noneruptive activity of the silicic caldera systems (Figure 10b): continuous pressurization of large magmatic reservoirs (Corbetti and Tullu Moje) or slow propagation of a viscous dike intrusion (Fentale). The other three signals are subsidence and associated with the compaction/loading of old volcanic products (Kone) or pore-pressure changes related to fluid migration (Aluto, Haledebi) (Figure 10b). Four of these six volcanoes (Aluto, Corbetti, Haledebi, and Tullu Moje) had similar patterns of deformation during the 2003–2010 InSAR survey (Biggs et al., 2011) (Table 1), which underlines that the processes causing unrest have been persistent for at least 12 years. Because of the increase in the temporal resolution (12 days for Sentinel-1), we were able to better detect seasonal signals for Aluto and Haledebi as well as small rate of displacements at Kone.

In the Kenyan-Tanzanian Rift, we detect deformation at only 2 of the 17 volcanic centers (Figure 10c). Subsidence at Olkaria is likely related to an increase in the production rate at the geothermal powerplant. Uplift at Suswa volcano started in mid-2018, and is likely to be caused by the build-up of pressure inside a central shallow reservoir. We do not detect any ground deformation for four volcanoes that previously showed unrest during the decade 1998–2008 (Table 1): Menengai, Longonot, Paka, and Ol Donyo Lengai. This absence of deformation suggests that the episodes of unrest in the Kenya-Tanzania rift are likely to be associated with shorter and/or more infrequent pulses of magmatic activity rather than long-lived processes as previously observed in the MER. Such behavior is confirmed by the detection of a new episode of uplift at Suswa volcano in mid-2018.

### 4.2. Ground Unrest and Volcanic Hazards

The eruptive cycles of continental rift volcanoes are poorly understood due to the lack of historical eruptions, making it difficult to forecast whether a period of unrest will be followed by an eruption. Satellite studies have been used to motivate additional geophysical investigations (Gottsmann et al., 2020; Samrock et al., 2018; Wilks et al., 2017) and have enabled us to interpret the processes causing the deformation. They have also prompted the first detailed hazard assessment for a continental rift volcano (Clarke et al., 2020; Tierz et al., 2020). However, detailed ground-based studies have only been conducted at a small number of volcanic centers and some deformation signals remain poorly understood (e.g., Haledebi, Gada Ale). It is important therefore to pursue the satellite monitoring of the EARS volcanic centers, and expand the program of ground-based studies, especially at those volcanoes showing persistent uplift.

In Ethiopia and Kenya, population exposure is high: over 70 million people live within 100-km radius of a Holocene volcano, meaning these countries ranked fifth and sixth in a recent global assessment of risk (Brown et al., 2015). Population density is particularly high in the central Main Ethiopian Rift, with 1.5 million people living within 30 km of the two silicic calderas showing persistent uplift: Corbetti and Tullu Moje. In Kenya, 100,000 people live <30 km from the only deforming system: Suswa. The population density in Afar is low but not insignificant—e.g., 37,000 people live <30 km from Dabbahu volcano (Global Volcanism Program, 2013), which was persistently uplifting during our survey. Although the number of fatalities due to earthquakes and eruptions in Africa has historically been much smaller than for droughts,

floods, or diseases (Mulugeta, 2019), the combination of high population exposure and vulnerability means a major volcanic eruption would have a large impact (Brown et al., 2015).

## 5. Conclusions

Our 5-year Sentinel-1 InSAR survey (2015–2020) in the EARS detected ground deformation at 14 volcanoes, which corresponds to about 20% of the Holocene active volcanoes in the region. Among them, the period of unrest was followed by an eruption only at one volcano, Erta Ale. For the first time, subsidence signals were identified at Kone (MER) and Olkaria (Kenya) and new episodes of uplift were detected at Tullu Moje (MER) and Suswa (Kenya). Our study underlines that ground deformation signals in the EARS are associated with a large range of processes having different spatial and time scales: long-lived uplift on restless calderas, rapid deformation (days/months) during magma intrusions, posteruptive deformation (uplift/subsidence) caused by the reequilibration of magma bodies, persistent subsidence caused by lava flow compaction and deformation related to pore-fluid pressure changes inside hydrothermal systems or geothermal fields.

## Data Availability Statement

Sentinel-1 interferograms processed by LiCSAR are available on the Centre for Environmental Data Analysis (CEDA) archive (http://data.ceda.ac.uk/neodc/comet/data/licsar_products). The data sets (unwrapped interferograms, coherence maps, and time series of displacements) that support the findings of this study were archived with the NERC's National Geoscience Data Centre (NGDC) and are available online (https://doi.org/10.5285/e7c3177b-4c73-4c20-961f-03afd09ccf69).

**Acknowledgments**
This research was funded by the NERC Large Grant RiftVolc (NE/L013649/1), NERC Innovation Grant (NE/S013970/1) and supported by the NERC Centre for the Observation and Modeling of Earthquakes, Volcanoes, and Tectonics (COMET, http://comet.nerc.ac.uk), a partnership between UK Universities and the British Geological Survey. We thank the three anonymous reviewers for their useful comments, which improved the manuscript.

## References

Agostini, A., Bonini, M., Corti, G., Sani, F., & Mazzarini, F. (2011). Fault architecture in the Main Ethiopian Rift and comparison with experimental models: Implications for rift evolution and Nubia–Somalia kinematics. *Earth and Planetary Science Letters*, *301*(3–4), 479–492.

Albino, F., & Biggs, J. (2021). *Processed InSAR images over the volcanoes of the East African Rift.*. British Geological Survey (Dataset). https://doi.org/10.5285/e7c3177b-4c73-4c20-961f-03afd09ccf69

Albino, F., Biggs, J., Yu, C., & Li, Z. (2020). Automated methods for detecting volcanic deformation using Sentinel-1 InSAR time series illustrated by the 2017–2018 unrest at Agung, Indonesia. *Journal of Geophysical Research: Solid Earth*, *125*, e2019JB017908. https://doi.org/10.1029/2019JB017908

Allis, R. G. (2000). Review of subsidence at Wairakei field, New Zealand. *Geothermics*, *29*(4–5), 455–478.

Amelung, F., Oppenheimer, C., Segall, P., & Zebker, H. (2000). Ground deformation near Gada Ale Volcano, Afar, observed by radar interferometry. *Geophysical Research Letters*, *27*(19), 3093–3096.

Araya, M. C., & Biggs, J. (2020). Episodic ground deformation associated with geothermal energy production at the Guayabo caldera, Costa Rica. *Journal of Volcanology and Geothermal Research*, *407*, 107110. https://doi.org/10.1016/j.jvolgeores.2020.107110

Ayele, A., Jacques, E., Kassim, M., Kidane, T., Omar, A., Tait, S., et al. (2007). The volcano–seismic crisis in Afar, Ethiopia, starting September 2005. *Earth and Planetary Science Letters*, *255*(1–2), 177–187.

Ayele, A., Keir, D., Ebinger, C., Wright, T. J., Stuart, G. W., Buck, W. R., et al. (2009). September 2005 mega-dike emplacement in the Manda-Harraro nascent oceanic rift (Afar depression). *Geophysical Research Letters*, *36*, L20306. https://doi.org/10.1029/2009GL039605

Baer, G., Hamiel, Y., Shamir, G., & Nof, R. (2008). Evolution of a magma-driven earthquake swarm and triggering of the nearby Oldoinyo Lengai eruption, as resolved by InSAR, ground observations and elastic modeling, East African Rift, 2007. *Earth and Planetary Science Letters*, *272*(1–2), 339–352.

Barbour, A. J., Evans, E. L., Hickman, S. H., & Eneva, M. (2016). Subsidence rates at the southern Salton Sea consistent with reservoir depletion. *Journal of Geophysical Research: Solid Earth*, *121*, 5308–5327. https://doi.org/10.1002/2016JB012903

Barnie, T., Keir, D., Hamling, I., Hofmann, B., Belachew, M., & Carn, S. (2016a). A multidisciplinary study of the final episode of the Manda Hararo dyke sequence, Ethiopia, and implications for trends in volcanism during the rifting cycle. *Geological Society, London, Special Publications*, *420*(1), 149–163.

Barnie, T., Oppenheimer, C., & Pagli, C. (2016b). Does the lava lake of Erta Ale volcano respond to regional magmatic and tectonic events? An investigation using Earth Observation data. *Geological Society, London, Special Publications*, *420*(1), 181–208.

Beauducel, F., Briole, P., & Froger, J.-L. (2000). Volcano-wide fringes in ERS synthetic aperture radar interferograms of Etna (1992–1998): Deformation or tropospheric effect? *Journal of Geophysical Research*, *105*(B7), 16391–16402.

Bekaert, D., Walters, R., Wright, T., Hooper, A., & Parker, D. (2015). Statistical comparison of InSAR tropospheric correction techniques. *Remote Sensing of Environment*, *170*, 40–47.

Biggs, J., Amelung, F., Gourmelen, N., Dixon, T. H., & Kim, S.-W. (2009a). InSAR observations of 2007 Tanzania rifting episode reveal mixed fault and dyke extension in an immature continental rift. *Geophysical Journal International*, *179*(1), 549–558.

Biggs, J., Anthony, E., & Ebinger, C. (2009b). Multiple inflation and deflation events at Kenyan volcanoes, East African Rift. *Geology*, *37*(11), 979–982.

Biggs, J., Bastow, I., Keir, D., & Lewi, E. (2011). Pulses of deformation reveal frequently recurring shallow magmatic activity beneath the Main Ethiopian Rift. *Geochemistry, Geophysics, Geosystems*, *12*, Q0AB10. https://doi.org/10.1029/2011GC003662

Biggs, J., Chivers, M., & Hutchinson, M. C. (2013). Surface deformation and stress interactions during the 2007–2010 sequence of earthquake, dyke intrusion and eruption in northern Tanzania. *Geophysical Journal International*, *195*(1), 16–26.
Biggs, J., Ebmeier, S., Aspinall, W., Lu, Z., Pritchard, M., Sparks, R., & Mather, T. (2014). Global link between deformation and volcanic eruption quantified by satellite imagery. *Nature Communications*, *5*(1), 3471.
Biggs, J., Robertson, E., & Cashman, K. (2016). The lateral extent of volcanic interactions during unrest and eruption. *Nature Geoscience*, *9*(4), 308–311.
Birhanu, Y., Wilks, M., Biggs, J., Kendall, J.-M., Ayele, A., & Lewi, E. (2018). Seasonal patterns of seismicity and deformation at the Alutu geothermal reservoir, Ethiopia, induced by hydrological loading. *Journal of Volcanology and Geothermal Research*, *356*, 175–182.
Bizouard, H., & Di Paola, G. (1978). Mineralogy of the Tullu Moje active volcanic area (Arussi: Ethiopian Rift valley). In E. R. Neumann, & I. B. Ramberg (Eds.), *Petrology and geochemistry of continental rifts* (Vol. 36, pp. 87–100). Berlin, Germany: Springer.
Bonatti, E., Emiliani, C., Ostlund, G., & Rydell, H. (1971). Final desiccation of the Afar rift, Ethiopia. *Science*, *172*(3982), 468–469.
Braddock, M., Biggs, J., Watson, I. M., Hutchison, W., Pyle, D. M., & Mather, T. A. (2017). Satellite observations of fumarole activity at Aluto volcano, Ethiopia: Implications for geothermal monitoring and volcanic hazard. *Journal of Volcanology and Geothermal Research*, *341*, 70–83.
Briole, P., Massonnet, D., & Delacourt, C. (1997). Post-eruptive deformation associated with the 1986–87 and 1989 lava flows of Etna detected by radar interferometry. *Geophysical Research Letters*, *24*(1), 37–40.
Brown, S. K., Auker, M., & Sparks, R. (2015). Populations around Holocene volcanoes and development of a Population Exposure Index. In *Global volcanic hazards and risk* (pp. 223–232). Cambridge, UK: Cambridge University Press.
Calais, E., d'Oreye, N., Albaric, J., Deschamps, A., Delvaux, D., Déverchere, J., et al. (2008). Strain accommodation by slow slip and dyking in a youthful continental rift, East Africa. *Nature*, *456*(7223), 783–787.
Caricchi, L., Biggs, J., Annen, C., & Ebmeier, S. (2014). The influence of cooling, crystallisation and re-melting on the interpretation of geodetic signals in volcanic systems. *Earth and Planetary Science Letters*, *388*, 166–174.
Carnec, C., & Fabriol, H. (1999). Monitoring and modeling land subsidence at the Cerro Prieto geothermal field, Baja California, Mexico, using SAR interferometry. *Geophysical Research Letters*, *26*(9), 1211–1214.
Carniel, R., Jolis, E. M., & Jones, J. (2010). A geophysical multi-parametric analysis of hydrothermal activity at Dallol, Ethiopia. *Journal of African Earth Sciences*, *58*(5), 812–819.
Cervelli, P., Segall, P., Amelung, F., Garbeil, H., Meertens, C., Owen, S., et al. (2002). The 12 September 1999 upper east rift zone dike intrusion at Kilauea volcano, Hawaii. *Journal of Geophysical Research*, *107*(B7), 2150. https://doi.org/10.1029/2001JB000602
Clarisse, L., Coheur, P.-F., Theys, N., Hurtmans, D., & Clerbaux, C. (2014). The 2011 Nabro eruption, a $SO_2$ plume height analysis using IASI measurements. *Atmospheric chemistry and physics*, *14*(6), 3095–3111. https://doi.org/10.5194/acp-14-3095-2014
Clarke, M., Woodhall, D., Allen, D., & Darling, G. (1990). *Geological, volcanological and hydrological controls on the occurrence of geothermal activity in the area surrounding Lake Naivasha, Kenya. Kenya*. Nairobi, Kenya: Ministry of Energy Report.
Clarke, B., Tierz, P., Calder, E., & Yirgu, G. (2020). Probabilistic volcanic hazard assessment for pyroclastic density currents from pumice cone eruptions at Aluto volcano, Ethiopia. *Frontiers in Earth Science*, *8*, 348.
Delacourt, C., Briole, P., & Achache, J. (1998). Tropospheric corrections of SAR interferograms with strong topography. Application to Etna. *Geophysical Research Letters*, *25*(15), 2849–2852.
Delgado, F., Pritchard, M., Samsonov, S., & Córdova, L. (2018). Renewed posteruptive uplift following the 2011–2012 rhyolitic eruption of Cordón Caulle (Southern Andes, Chile): Evidence for transient episodes of magma reservoir recharge during 2012–2018. *Journal of Geophysical Research: Solid Earth*, *123*, 9407–9429. https://doi.org/10.1029/2018JB016240
Delgado, F., Pritchard, M. E., Basualto, D., Lazo, J., Córdova, L., & Lara, L. E. (2016). Rapid reinflation following the 2011–2012 rhyodacite eruption at Cordón Caulle volcano (Southern Andes) imaged by InSAR: Evidence for magma reservoir refill. *Geophysical Research Letters*, *43*, 9552–9562. https://doi.org/10.1002/2016GL070066
Del Gaudio, C., Aquino, I., Ricciardi, G., Ricco, C., & Scandone, R. (2010). Unrest episodes at Campi Flegrei: A reconstruction of vertical ground movements during 1905–2009. *Journal of Volcanology and Geothermal Research*, *195*(1), 48–56.
Doubre, C., & Peltzer, G. (2007). Fluid-controlled faulting process in the Asal Rift, Djibouti, from 8 yr of radar interferometry observations. *Geology*, *35*(1), 69–72.
Ebinger, C., Keir, D., Ayele, A., Calais, E., Wright, T., Belachew, M., et al. (2008). Capturing magma intrusion and faulting processes during continental rupture: Seismicity of the Dabbahu (Afar) rift. *Geophysical Journal International*, *174*(3), 1138–1152.
Ebmeier, S., Andrews, B., Araya, M., Arnold, D., Biggs, J., & Cooper, C. (2018). Synthesis of global satellite observations of magmatic and volcanic deformation: Implications for volcano monitoring and the lateral extent of magmatic domains. *Journal of Applied Volcanology*, *7*(1), 2.
Ebmeier, S., Biggs, J., Mather, T., & Amelung, F. (2013). Applicability of InSAR to tropical volcanoes: Insights from Central America. *Geological Society, London, Special Publications*, *380*(1), 15–37.
Ebmeier, S., Biggs, J., Mather, T., Elliott, J., Wadge, G., & Amelung, F. (2012). Measuring large topographic change with InSAR: Lava thicknesses, extrusion rate and subsidence rate at Santiaguito volcano, Guatemala. *Earth and Planetary Science Letters*, *335*, 216–225.
Fialko, Y., & Simons, M. (2000). Deformation and seismicity in the Coso geothermal area, Inyo County, California: Observations and modeling using satellite radar interferometry. *Journal of Geophysical Research*, *105*(B9), 21781–21793.
Fontijn, K., McNamara, K., Tadesse, A. Z., Pyle, D. M., Dessalegn, F., Hutchison, W., et al. (2018). Contrasting styles of post-caldera volcanism along the Main Ethiopian Rift: Implications for contemporary volcanic hazards. *Journal of Volcanology and Geothermal Research*, *356*, 90–113.
Global Volcanism Program. (2013). *Volcanoes of the World, 4.4.8.* Retrieved from https://doi.org/10.5479/si.GVP.VOTW4-2013
Goitom, B., Oppenheimer, C., Hammond, J. O., Grandin, R., Barnie, T., & Donovan, A. (2015). First recorded eruption of Nabro volcano, Eritrea, 2011. *Bulletin of Volcanology*, *77*(10), 85.
Gottsmann, J., Biggs, J., Lloyd, R., Biranhu, Y., & Lewi, E. (2020). Ductility and compressibility accommodate high magma flux beneath a silicic continental rift caldera: Insights from Corbetti caldera (Ethiopia). *Geochemistry, Geophysics, Geosystems*, *21*, e2020GC008952. https://doi.org/10.1029/2020GC008952
Grandin, R., Jacques, E., Nercessian, A., Ayele, A., Doubre, C., Socquet, A., et al. (2011). Seismicity during lateral dike propagation: Insights from new data in the recent Manda Hararo–Dabbahu rifting episode (Afar, Ethiopia). *Geochemistry, Geophysics, Geosystems*, *12*, Q0AB08. https://doi.org/10.1029/2010GC003434
Grandin, R., Socquet, A., Binet, R., Klinger, Y., Jacques, E., & de Chabalier, J.-B. (2009). September 2005 Manda Hararo-Dabbahu rifting event, Afar (Ethiopia): Constraints provided by geodetic data. *Journal of Geophysical Research*, *114*, B08404. https://doi.org/10.1029/2008JB005843

Grandin, R., Socquet, A., Doin, M.-P., Jacques, E., de Chabalier, J.-B., & King, G. (2010a). Transient rift opening in response to multiple dike injections in the Manda Hararo rift (Afar, Ethiopia) imaged by time-dependent elastic inversion of interferometric synthetic aperture radar data. *Journal of Geophysical Research*, *115*, B09403. https://doi.org/10.1029/2009JB006883

Grandin, R., Socquet, A., Jacques, E., Mazzoni, N., de Chabalier, J.-B., & King, G. (2010b). Sequence of rifting in Afar, Manda-Hararo rift, Ethiopia, 2005–2009: Time-space evolution and interactions between dikes from interferometric synthetic aperture radar and static stress change modeling. *Journal of Geophysical Research*, *115*, B10413. https://doi.org/10.1029/2009JB000815

Greenfield, T., Keir, D., Kendall, J.-M., & Ayele, A. (2019a). Low-frequency earthquakes beneath Tullu Moye volcano, Ethiopia, reveal fluid pulses from shallow magma chamber. *Earth and Planetary Science Letters*, *526*, 115782.

Greenfield, T., Keir, D., Kendall, J.-M., & Ayele, A. (2019b). Seismicity of the Bora-Tullu Moye volcanic field, 2016–2017. *Geochemistry, Geophysics, Geosystems*, *20*, 548–570. https://doi.org/10.1029/2018GC007648

Gudmundsson, A. (1995). Infrastructure and mechanics of volcanic systems in Iceland. *Journal of Volcanology and Geothermal Research*, *64*(1–2), 1–22.

Hamling, I., Ayele, A., Bennati, L., Calais, E., Ebinger, C. J., Keir, D., et al. (2009). Geodetic observations of the ongoing Dabbahu rifting episode: New dyke intrusions in 2006 and 2007. *Geophysical Journal International*, *178*(2), 989–1003.

Hamling, I., Williams, C., & Hreinsdóttir, S. (2016). Depressurization of a hydrothermal system following the August and November 2012 Te Maari eruptions of Tongariro, New Zealand. *Geophysical Research Letters*, *43*, 168–175. https://doi.org/10.1002/2015GL067264

Hamling, I., Wright, T., Calais, E., Lewi, E., & Fukahata, Y. (2014). InSAR observations of post-rifting deformation around the Dabbahu rift segment, Afar, Ethiopia. *Geophysical Journal International*, *197*(1), 33–49.

Hamlyn, J., Keir, D., Wright, T. J., Neuberg, J. W., Goitom, B., Hammond, J. O., et al. (2014). Seismicity and subsidence following the 2011 Nabro eruption, Eritrea: Insights into the plumbing system of an off-rift volcano. *Journal of Geophysical Research: Solid Earth*, *119*, 8267–8282. https://doi.org/10.1002/2014JB011395

Hamlyn, J., Wright, T., Walters, R., Pagli, C., Sansosti, E., & Casu, F. (2018). What causes subsidence following the 2011 eruption at Nabro (Eritrea)? *Progress in Earth and Planetary Science*, *5*(1), 31.

Harris, I., Osborn, T. J., Jones, P., & Lister, D. (2020). Version 4 of the CRU TS monthly high-resolution gridded multivariate climate dataset. *Scientific Data*, *7*(1), 109.

Harris, W. C. (1844). The highlands of Aethiopia. In Three volumes (Vol. 2). Harlow, UK: Longman, Brown, Green and Longmans.

Henderson, S. T., Delgado, F., Elliott, J., Pritchard, M. E., & Lundgren, P. R. (2017). Decelerating uplift at Lazufre volcanic center, Central Andes, from AD 2010 to 2016, and implications for geodetic models. *Geosphere*, *13*(5), 1489–1505.

Hjartardóttir, Á. R., Einarsson, P., Bramham, E., & Wright, T. J. (2012). The Krafla fissure swarm, iceland, and its formation by rifting events. *Bulletin of Volcanology*, *74*(9), 2139–2153.

Hutchison, W., Biggs, J., Mather, T. A., Pyle, D. M., Lewi, E., Yirgu, G., et al. (2016a). Causes of unrest at silicic calderas in the East African Rift: New constraints from InSAR and soil-gas chemistry at Aluto volcano, Ethiopia. *Geochemistry, Geophysics, Geosystems*, *17*, 3008–3030. https://doi.org/10.1002/2016GC006395

Hutchison, W., Fusillo, R., Pyle, D. M., Mather, T. A., Blundy, J. D., & Biggs, J. (2016b). A pulse of mid-Pleistocene rift volcanism in Ethiopia at the dawn of modern humans. *Nature Communications*, *7*(1), 13192.

Hutchison, W., Mather, T. A., Pyle, D. M., Biggs, J., & Yirgu, G. (2015). Structural controls on fluid pathways in an active rift system: A case study of the Aluto volcanic complex. *Geosphere*, *11*(3), 542–562.

Hutchison, W., Pyle, D. M., Mather, T. A., Yirgu, G., Biggs, J., Cohen, B. E., et al. (2016c). The eruptive history and magmatic evolution of Aluto volcano: New insights into silicic peralkaline volcanism in the Ethiopian rift. *Journal of Volcanology and Geothermal Research*, *328*, 9–33.

Kebede, S. (2016). Country update on geothermal exploration and development in Ethiopia. In *Proceedings, 6th African Rift Geothermal Conference* (pp. 1–8).

Kebede, S., Mamo, T., & Abebe, T. (1985). Explanation to the geological map of Aluto-Langano geothermal area (Tech. Rep.). Ethiopia: Ethiopian Institute of Geological Surveys Addis Ababa.

Keir, D., Hamling, I. J., Ayele, A., Calais, E., Ebinger, C., Wright, T. J., et al. (2009). Evidence for focused magmatic accretion at segment centers from lateral dike injections captured beneath the Red Sea rift in Afar. *Geology*, *37*(1), 59–62.

Keir, D., Pagli, C., Bastow, I. D., & Ayele, A. (2011). The magma-assisted removal of Arabia in Afar: Evidence from dike injection in the Ethiopian rift captured using InSAR and seismicity. *Tectonics*, *30*, TC2008. https://doi.org/10.1029/2010TC002785

Kendall, J.-M., Stuart, G., Ebinger, C., Bastow, I., & Keir, D. (2005). Magma-assisted rifting in Ethiopia. *Nature*, *433*(7022), 146–148.

Koros, W. K., & Agustin, F. (2017). Subsidence surveys at Olkaria geothermal field, Kenya. *Journal of Spatial Science*, *62*(1), 195–205.

Lavayssière, A., Greenfield, T., Keir, D., Ayele, A., & Kendall, J.-M. (2019). Local seismicity near the actively deforming Corbetti volcano in the Main Ethiopian Rift. *Journal of Volcanology and Geothermal Research*, *381*, 227–237.

Lazecký, M., Spaans, K., González, P. J., Maghsoudi, Y., Morishita, Y., & Albino, F. (2020). LiCSAR: An automatic InSAR tool for measuring and monitoring tectonic and volcanic activity. *Remote Sensing*, *12*(15), 2430.

Lee, H., Muirhead, J. D., Fischer, T. P., Ebinger, C. J., Kattenhorn, S. A., Sharp, Z. D., & Kianji, G. (2016). Massive and prolonged deep carbon emissions associated with continental rifting. *Nature Geoscience*, *9*(2), 145–149.

Le Mével, H., Gregg, P. M., & Feigl, K. L. (2016). Magma injection into a long-lived reservoir to explain geodetically measured uplift: Application to the 2007–2014 unrest episode at Laguna del Maule volcanic field, Chile. *Journal of Geophysical Research: Solid Earth*, *121*, 6092–6108. https://doi.org/10.1002/2016JB013066

Lengliné, O., Marsan, D., Got, J.-L., Pinel, V., Ferrazzini, V., & Okubo, P. G. (2008). Seismicity and deformation induced by magma accumulation at three basaltic volcanoes. *Journal of Geophysical Research*, *113*, B12305. https://doi.org/10.1029/2008JB005937

Lloyd, R., Biggs, J., Birhanu, Y., Wilks, M., Gottsmann, J., Kendall, J.-M., et al. (2018a). Sustained uplift at a continental rift caldera. *Journal of Geophysical Research: Solid Earth*, *123*, 5209–5226. https://doi.org/10.1029/2018JB015711

Lloyd, R., Biggs, J., Wilks, M., Nowacki, A., Kendall, J.-M., Ayele, A., et al. (2018b). Evidence for cross rift structural controls on deformation and seismicity at a continental rift caldera. *Earth and Planetary Science Letters*, *487*, 190–200.

Lohman, R. B., & Simons, M. (2005). Some thoughts on the use of InSAR data to constrain models of surface deformation: Noise structure and data downsampling. *Geochemistry, Geophysics, Geosystems*, *6*, Q01007. https://doi.org/10.1029/2004GC000841

López-García, J. M., Moreira, D., Benzerara, K., Grunewald, O., & López-García, P. (2020). Origin and evolution of the halo-volcanic complex of Dallol: Proto-volcanism in Northern Afar (Ethiopia). *Frontiers in Earth Science*, *7*, 351.

Lowenstern, J. B., Smith, R. B., & Hill, D. P. (2006). Monitoring super-volcanoes: Geophysical and geochemical signals at Yellowstone and other large caldera systems. *Philosophical Transactions of the Royal Society A: Mathematical, Physical and Engineering Sciences*, *364*(1845), 2055–2072.

Lu, Z., & Dzurisin, D. (2014). InSAR imaging of Aleutian volcanoes. In *InSAR imaging of aleutian volcanoes* (pp. 87–345). Berlin, Germany: Springer.
Mangi, P. M. (2018). Geothermal development in Kenya Country updates. In *Proceedings of the 7th African Rift geothermal conference, Kigali, Rwanda*.
Martin-Jones, C. M., Lane, C. S., Pearce, N. J., Smith, V. C., Lamb, H. F., Schaebitz, F., et al. (2017). Recurrent explosive eruptions from a high-risk Main Ethiopian Rift volcano throughout the Holocene. *Geology*, *45*(12), 1127–1130.
Massonnet, D., Holzer, T., & Vadon, H. (1997). Land subsidence caused by the East Mesa geothermal field, California, observed using SAR interferometry. *Geophysical Research Letters*, *24*(8), 901–904.
McNamara, K., Cashman, K., Rust, A., Fontijn, K., Chalié, F., Tomlinson, E. L., & Yirgu, G. (2018). Using lake sediment cores to improve records of volcanism at Aluto volcano in the Main Ethiopian Rift. *Geochemistry, Geophysics, Geosystems*, *19*, 3164–3188. https://doi.org/10.1029/2018GC007686
Moore, C., Wright, T., Hooper, A., & Biggs, J. (2019). The 2017 Eruption of Erta'Ale Volcano, Ethiopia: Insights into the shallow axial plumbing system of an incipient mid-ocean ridge. *Geochemistry, Geophysics, Geosystems*, *20*, 727–5743. https://doi.org/10.1029/2019GC008692
Mossop, A., & Segall, P. (1997). Subsidence at the Geysers geothermal field, N. California from a comparison of GPS and leveling surveys. *Geophysical Research Letters*, *24*(14), 1839–1842.
Mulugeta, G. (2019). Overview of the impact of hazards and disasters in Africa, In G. Mulugeta & T. Simelane (Eds.), *Natural and Human-Induced Hazards and Disasters in Africa*. Pretoria: Africa Institute of South Africa.
Narasimhan, T., & Goyal, K. (1984). Subsidence due to geothermal fluid withdrawal. Man-induced land subsidence. *Reviews in Engineering Geology*, *6*, 35–36.
Narita, S., & Murakami, M. (2018). Shallow hydrothermal reservoir inferred from post-eruptive deflation at Ontake Volcano as revealed by PALSAR-2 InSAR. *Earth, Planets and Space*, *70*(1), 191.
Newman, A., Dixon, T. H., Ofoegbu, G., & Dixon, J. (2001). Geodetic and seismic constraints on recent activity at Long Valley Caldera, California: Evidence for viscoelastic rheology. *Journal of Volcanology and Geothermal Research*, *105*(3), 183–206.
Nobile, A., Pagli, C., Keir, D., Wright, T. J., Ayele, A., Ruch, J., & Acocella, V. (2012). Dike-fault interaction during the 2004 Dallol intrusion at the northern edge of the Erta Ale Ridge (Afar, Ethiopia). *Geophysical Research Letters*, *39*, L19305. https://doi.org/10.1029/2012GL053152
Nooner, S. L., Bennati, L., Calais, E., Buck, W. R., Hamling, I. J., Wright, T. J., & Lewi, E. (2009). Post-rifting relaxation in the Afar region, Ethiopia. *Geophysical Research Letters*, *36*, L21308. https://doi.org/10.1029/2009GL040502
Nowacki, A., Wilks, M., Kendall, J.-M., Biggs, J., & Ayele, A. (2018). Characterising hydrothermal fluid pathways beneath Aluto volcano, Main Ethiopian Rift, using shear wave splitting. *Journal of Volcanology and Geothermal Research*, *356*, 331–341.
Omenda, P. (1998). The geology and structural controls of the Olkaria geothermal system, Kenya. *Geothermics*, *27*(1), 55–74.
Omenda, P., & Teklemariam, M. (2010). Overview of geothermal resource utilization in the East African Rift System. Presented at *Short Course V on exploration for geothermal resources* (pp. 1–11). Lake Bogoria and Lake Naivasha, Kenya: UNU-GTP, GDC and KenGen.
Oppenheimer, C., & Francis, P. (1997). Remote sensing of heat, lava and fumarole emissions from Erta'Ale volcano, Ethiopia. *International Journal of Remote Sensing*, *18*(8), 1661–1692.
Pagli, C., Wang, H., Wright, T. J., Calais, E., & Lewi, E. (2014). Current plate boundary deformation of the Afar rift from a 3-D velocity field inversion of InSAR and GPS. *Journal of Geophysical Research: Solid Earth*, *119*, 8562–8575. https://doi.org/10.1002/2014JB011391
Pagli, C., Wright, T. J., Ebinger, C. J., Yun, S.-H., Cann, J. R., Barnie, T., & Ayele, A. (2012). Shallow axial magma chamber at the slow-spreading Erta Ale Ridge. *Nature Geoscience*, *5*(4), 284–288.
Parker, A. L., Biggs, J., Walters, R. J., Ebmeier, S. K., Wright, T. J., Teanby, N. A., & Lu, Z. (2015). Systematic assessment of atmospheric uncertainties for InSAR data at volcanic arcs using large-scale atmospheric models: Application to the Cascade volcanoes, United States. *Remote Sensing of Environment*, *170*, 102–114.
Pinel, V., Hooper, A., De la Cruz-Reyna, S., Reyes-Davila, G., Doin, M., & Bascou, P. (2011). The challenging retrieval of the displacement field from InSAR data for andesitic stratovolcanoes: Case study of Popocatepetl and Colima Volcano, Mexico. *Journal of Volcanology and Geothermal Research*, *200*(1–2), 49–61.
Poland, M., Bürgmann, R., Dzurisin, D., Lisowski, M., Masterlark, T., Owen, S., & Fink, J. (2006). Constraints on the mechanism of long-term, steady subsidence at Medicine Lake volcano, northern California, from GPS, leveling, and InSAR. *Journal of Volcanology and Geothermal Research*, *150*(1–3), 55–78.
Pyle, D. M., Mather, T. A., & Biggs, J. (2013). Remote sensing of volcanoes and volcanic processes: Integrating observation and modelling–introduction. *Geological Society, London, Special Publications*, *380*(1), 1–13.
Rampey, M. L., Oppenheimer, C., Pyle, D. M., & Yirgu, G. (2010). Caldera-forming eruptions of the Quaternary Kone volcanic complex, Ethiopia. *Journal of African Earth Sciences*, *58*(1), 51–66.
Rapprich, V., Žáček, V., Verner, K., Erban, V., Goslar, T., Bekele, Y., et al. (2016). Wendo Koshe Pumice: The latest Holocene silicic explosive eruption product of the Corbetti volcanic system (southern Ethiopia). *Journal of Volcanology and Geothermal Research*, *310*, 159–171.
Reath, K., Pritchard, M., Biggs, J., Andrews, B., Ebmeier, S., Bagnardi, M., et al. (2020). Using conceptual models to relate multiparameter satellite data to subsurface volcanic processes in Latin America. *Geochemistry, Geophysics, Geosystems*, *21*, e2019GC008494. https://doi.org/10.1029/2019GC008494
Remy, D., Bonvalot, S., Briole, P., & Murakami, M. (2003). Accurate measurements of tropospheric effects in volcanic areas from SAR interferometry data: Application to Sakurajima volcano (Japan). *Earth and Planetary Science Letters*, *213*(3–4), 299–310.
Rivalta, E. (2010). Evidence that coupling to magma chambers controls the volume history and velocity of laterally propagating intrusions. *Journal of Geophysical Research*, *115*, B07203. https://doi.org/10.1029/2009JB006922
Robertson, E., Biggs, J., Edmonds, M., Clor, L., Fischer, T. P., Vye-Brown, C., et al. (2016). Diffuse degassing at Longonot volcano, Kenya: Implications for CO2 flux in continental rifts. *Journal of Volcanology and Geothermal Research*, *327*, 208–222.
Rotich, A. K. (2016). KenGen geothermal development status and future expansion plants. In *Proceedings, 6th African Rift geothermal Conference, Addis Ababa, Ethiopia, 2nd–4th November* (pp. 1–8).
Rubin, A. M. (1990). A comparison of rift-zone tectonics in Iceland and Hawaii. *Bulletin of Volcanology*, *52*(4), 302–319.
Rubin, A. M. (1992). Dike-induced faulting and graben subsidence in volcanic rift zones. *Journal of Geophysical Research*, *97*(B2), 1839–1858.
Samrock, F., Grayver, A. V., Eysteinsson, H., & Saar, M. O. (2018). Magnetotelluric image of transcrustal magmatic system beneath the Tulu Moye geothermal prospect in the Ethiopian Rift. *Geophysical Research Letters*, *45*, 12847–12855. https://doi.org/10.1029/2018GL080333
Sarychikhina, O., Glowacka, E., Mellors, R., & Vidal, F. S. (2011). Land subsidence in the Cerro Prieto Geothermal Field, Baja California, Mexico, from 1994 to 2005: An integrated analysis of DInSAR, leveling and geological data. *Journal of Volcanology and Geothermal Research*, *204*(1–4), 76–90.

Schmidt, D. A., & Bürgmann, R. (2003). Time-dependent land uplift and subsidence in the Santa Clara valley, California, from a large interferometric synthetic aperture radar data set. *Journal of Geophysical Research*, *108*(B9), 2416. https://doi.org/10.1029/2002JB002267

Segall, P. (2016). Repressurization following eruption from a magma chamber with a viscoelastic aureole. *Journal of Geophysical Research: Solid Earth*, *121*, 8501–8522. https://doi.org/10.1002/2016JB013597

Simiyu, S. M. (2010). Status of geothermal exploration in Kenya and future plans for its development. In *Proceedings world geothermal congress* (pp. 25–29). International Geothermal Association, Bali, Indonesia, 25–29 April 2010

Stephens, K. J., Wauthier, C., Bussard, R. C., Higgins, M., & LaFemina, P. C. (2020). Assessment of mitigation strategies for tropospheric phase contributions to InSAR time-series datasets over two Nicaraguan Volcanoes. *Remote Sensing*, *12*(5), 782.

Stevens, N., Wadge, G., Williams, C., Morley, J., Muller, J.-P., Murray, J., & Upton, M. (2001). Surface movements of emplaced lava flows measured by synthetic aperture radar interferometry. *Journal of Geophysical Research*, *106*(B6), 11293–11313.

Temtime, T., Biggs, J., Lewi, E., & Ayele, A. (2020). Evidence for Active Rhyolitic Dyke Intrusion in the Northern Main Ethiopian Rift from the 2015 Fentale Seismic Swarm. *Geochemistry, Geophysics, Geosystems*, *21*, e2019GC008550. https://doi.org/10.1029/2019GC008550

Temtime, T., Biggs, J., Lewi, E., Hamling, I., Wright, T., & Ayele, A. (2018). Spatial and temporal patterns of deformation at the Tendaho geothermal prospect, Ethiopia. *Journal of Volcanology and Geothermal Research*, *357*, 56–67.

Tierz, P., Clarke, B., Calder, E. S., Dessalegn, F., Lewi, E., Yirgu, G., et al. (2020). Event trees and epistemic uncertainty in long-term volcanic hazard assessment of rift volcanoes: The example of Aluto (Central Ethiopia). *Geochemistry, Geophysics, Geosystems*, *21*, e2020GC009219. https://doi.org/10.1029/2020GC009219

Usai, S. (2003). A least squares database approach for SAR interferometric data. *IEEE Transactions on Geoscience and Remote Sensing*, *41*(4), 753–760.

Werner, C., Wegmüller, U., Strozzi, T., & Wiesmann, A. (2000). Gamma SAR and interferometric processing software. In *Proceedings of the Ers-Envisat symposium, Gothenburg, Sweden* (pp. 1620).

White, J. C., Espejel-García, V. V., Anthony, E. Y., & Omenda, P. (2012). Open system evolution of peralkaline trachyte and phonolite from the Suswa volcano, Kenya rift. *Lithos*, *152*, 84–104.

Wiart, P., & Oppenheimer, C. (2005). Large magnitude silicic volcanism in north Afar: The Nabro volcanic range and Maalalta volcano. *Bulletin of Volcanology*, *67*(2), 99–115.

Wilks, M., Kendall, J.-M., Nowacki, A., Biggs, J., Wookey, J., Birhanu, Y., et al. (2017). Seismicity associated with magmatism, faulting and hydrothermal circulation at Aluto Volcano, Main Ethiopian Rift. *Journal of Volcanology and Geothermal Research*, *340*, 52–67.

Wilks, M., Rawlinson, N., Kendall, J.-M., Nowacki, A., Biggs, J., Ayele, A., & Wookey, J. (2020). The Coupled magmatic and hydrothermal systems of the restless Aluto Caldera, Ethiopia. *Frontiers in Earth Science*, *8*. https://doi.org/10.3389/feart.2020.579699

Wright, T., Ebinger, C., Biggs, J., Ayele, A., Yirgu, G., Keir, D., & Stork, A. (2006). Dyke-maintained rift segmentation at continental rupture–the 2005 Dabbahu (Afar) rifting episode. *Nature*, *442*(20), 291–294.

Xu, W., Rivalta, E., & Li, X. (2017). Magmatic architecture within a rift segment: Articulate axial magma storage at Erta Ale volcano, Ethiopia. *Earth and Planetary Science Letters*, *476*, 79–86.

Xu, W., Xie, L., Aoki, Y., Rivalta, E., & Jónsson, S. (2020). Volcano-wide deformation after the 2017 Erta Ale dike intrusion, Ethiopia, observed with radar interferometry. *Journal of Geophysical Research: Solid Earth*, *125*, e2020JB019562. https://doi.org/10.1029/2020JB019562

Yagüe-Martínez, N., Prats-Iraola, P., Gonzalez, F. R., Brcic, R., Shau, R., Geudtner, D., et al. (2016). Interferometric processing of Sentinel-1 TOPS data. *IEEE Transactions on Geoscience and Remote Sensing*, *54*(4), 2220–2234.

Yip, S., Biggs, J., & Albino, F. (2019). Reevaluating volcanic deformation using atmospheric corrections: Implications for the magmatic system of Agung Volcano, Indonesia. *Geophysical Research Letters*, *46*, 13704–13711. https://doi.org/10.1029/2019GL085233

Yirgu, G., Ayalew, D., & Ayele, A. (2006). Recent seismovolcanic crisis in northern Afar, Ethiopia. *Eos, Transactions American Geophysical Union*, *87*(33), 325–329.

Clarisse, L., Coheur, P.-F., Theys, N., Hurtmans, D., & Clerbaux, C. (2014). The 2011 Nabro eruption, a SO2 plume height analysis using IASI measurements. *Atmospheric chemistry and physics*, *14*(6), 3095–3111. https://doi.org/10.5194/acp-14-3095-2014.